

## NUMERICAL MAGNETOHYDRODYNAMICS IN ASTROPHYSICS: ALGORITHM AND TESTS FOR ONE-DIMENSIONAL FLOW

DONGSU RYU

Princeton University Observatory; and Department of Astronomy and Space Science,  
 Chungnam National University, Daejeon 305-764, (South) Korea

AND

T. W. JONES

School of Physics and Astronomy, University of Minnesota, Minneapolis, MN 55455

Received 1994 May 5; accepted 1994 September 30

### ABSTRACT

We describe a numerical code to solve the equations for ideal magnetohydrodynamics (MHD). It is based on an explicit finite difference scheme on an Eulerian grid, called the total variation diminishing (TVD) scheme, which is a second-order-accurate extension of the Roe-type upwind scheme. We also describe a nonlinear Riemann solver for ideal MHD, which includes rarefactions as well as shocks. The numerical code and the Riemann solver have been used to test each other.

Extensive tests encompassing all the possible ideal MHD structures with planar symmetries (i.e., one-dimensional flows) are presented. These include those for which the field structure is two dimensional (i.e., those flows often called “ $1 + \frac{1}{2}$  dimensional”) as well as those for which the magnetic field plane rotates (i.e., those flows often called “ $1 + \frac{1}{2} + \frac{1}{2}$  dimensional”). Results indicate that the code can resolve strong fast, slow, and magnetosonic shocks within two to four cells, but more cells are required if shocks become weak. With proper steepening, we could resolve rotational discontinuities within three to five cells. However, without successful implementation of steepening, contact discontinuities are resolved with  $\sim 10$  cells and tangential discontinuities are resolved with  $\sim 15$  cells.

Our tests confirm that slow compound structures with two-dimensional magnetic fields are composed of intermediate shocks (so-called 2–4 intermediate shocks) followed by slow rarefaction waves. Finally, tests demonstrate that in two-dimensional magnetohydrodynamics, fast compound structures, which are composed of intermediate shocks (so-called 1–3 intermediate shocks) preceded by fast rarefaction waves, are also possible.

*Subject headings:* hydromagnetics — MHD — methods: numerical — shock waves

### 1. INTRODUCTION

Many astronomical objects as diverse as planets, stars, and galaxies all possess magnetic fields that have important implications for their dynamics and evolution. However, in many objects including Earth, the ohmic dissipation time  $t_D = L/\eta^2$  ( $\eta$  is the electric resistivity) is smaller than their ages. So, their magnetic fields should be continuously generated by some dynamo activity; otherwise, the observed strength cannot be maintained. The dynamo activity involves patterns of magnetohydrodynamic (MHD) flows (for example, the interaction of differential rotation and convection as in some stars or accretion disks) needed to produce spatially coherent magnetic fields of large scale. However, such flows are usually highly nonlinear, so with several exceptions, analytic approaches to understand dynamo theory and the origin of the magnetic field have failed (for review and further references, see Parker 1979).

There are numerous other examples of astrophysical problems whose solution demands an ability to follow the nonlinear evolution of MHD flows. Although full understanding of these applications will ultimately require multidimensional computations, for some of them plane-symmetric nonlinear MHD is still an extremely valuable and new step forward. A case in point is the study of cosmic-ray-modified shocks. For more than 15 years, diffusive transport of high-energy particles mediated by Alfvén waves has been recognized as the prime candidate for the acceleration of cosmic rays and that the processes involve complex nonlinear feedback between the particles and a conducting, magnetized fluid. Yet until very recently only simplified, analytic steady state MHD treatments of this problem have appeared.

With the appearance of fast supercomputers, it has become possible to study such MHD flows numerically. However, the development of numerical techniques to solve MHD equations has been slower, due to the intrinsic complexity of the MHD flows. For instance, until now most numerical schemes to solve compressible MHD equations have been based on the methods using artificial viscosity (e.g., DeVore 1991; Lind, Payne, & Meier 1991; Stone et al. 1992; Stone & Norman 1992), while schemes to solve compressible hydrodynamic equations have been based on methods using more sophisticated linear or nonlinear Riemann solvers (e.g., Roe 1981; Colella & Woodward 1984). It is rather recent that Brio & Wu (1988, hereafter BW), Zachary & Colella (1992), and Zachary, Malagoli, & Colella (1994) developed schemes for MHD equations based on linear Riemann solvers and Dai & Woodward (1994a, hereafter DW) and Dai & Woodward (1994b) developed one based on a nonlinear Riemann solver.

In this paper, we describe a one-dimensional code to solve numerically the ideal MHD equations. It is based on an explicit second-order-accurate finite difference scheme on an Eulerian grid, called the total variation diminishing (TVD) scheme, which was originally developed for numerical hydrodynamics by Harten (1983). It utilizes a Roe-type “linear” Riemann solver described in BW.

Here, we do not attempt to describe the theoretical philosophy of the scheme, which can be found in Harten (1983) and BW. Instead, we focus on the description of the procedure necessary to write the code and the test results for its performance.

We also describe a “nonlinear” Riemann solver for ideal magnetohydrodynamics (MHDs) which has been developed to provide analytic solutions for shock tube tests of the code. It has been built by following a procedure similar to that in DW, but using initial guesses with the linear eigenvectors from BW and Zachary & Colella (1992).

The paper is organized in the following way. In § 2 we describe the step-by-step procedure for the code. In § 3 we describe the nonlinear Riemann solver in detail. We intend to provide detailed descriptions of the code and the nonlinear Riemann solver so others can recover them by following the descriptions. Tests using shock tubes are presented in § 4 to demonstrate the ability of the code to capture discontinuities as well as to follow smooth flows. The tests also serve to show the performance of the nonlinear Riemann solver. Finally, discussion follows in § 5, including the possible existence of fast compound structures as well as slow compound structures for two-dimensional magnetic field patterns.

## 2. TVD CODE FOR IDEAL MHDs

### 2.1. Ideal MHD Equations

The subject of MHDs describes the dynamics of electrically conducting fluids in the presence of magnetic fields. The MHD equations represent coupling of the equations of fluid dynamics with the Maxwell's equations of electrodynamics. By neglecting the displacement current, the separation between ions and electrons, and the effects of electrical resistivity, viscosity, and thermal conduction, we get the following ideal MHD equations:

$$\frac{\partial \rho}{\partial t} + \nabla \cdot (\rho \mathbf{v}) = 0, \quad (2.1)$$

$$\frac{\partial \mathbf{v}}{\partial t} + \mathbf{v} \cdot \nabla \mathbf{v} + \frac{1}{\rho} \nabla \rho - \frac{1}{\rho} (\nabla \times \mathbf{B}) \times \mathbf{B} = 0, \quad (2.2)$$

$$\frac{\partial p}{\partial t} + \mathbf{v} \cdot \nabla p + \gamma p \nabla \cdot \mathbf{v} = 0, \quad (2.3)$$

$$\frac{\partial \mathbf{B}}{\partial t} - \nabla \times (\mathbf{v} \times \mathbf{B}) = 0, \quad (2.4)$$

with an additional constraint  $\nabla \cdot \mathbf{B} = 0$  for the absence of magnetic monopole (for details, see Shu 1992). Here, we have chosen units so that factor of  $4\pi$  does not appear in the equations.

For plane-symmetric, or one-dimensional flows exhibiting variation along the  $x$ -direction, the equations (2.1)–(2.4) can be written in conservative form as

$$\frac{\partial \mathbf{q}}{\partial t} + \frac{\partial \mathbf{F}}{\partial x} = 0, \quad (2.5)$$

$$\mathbf{q} = \begin{pmatrix} \rho \\ \rho v_x \\ \rho v_y \\ \rho v_z \\ B_y \\ B_z \\ E \end{pmatrix}, \quad (2.6)$$

$$\mathbf{F} = \begin{pmatrix} \rho v_x \\ \rho v_x^2 + p^* - B_x^2 \\ \rho v_x v_y - B_x B_y \\ \rho v_x v_z - B_x B_z \\ B_y v_x - B_x v_y \\ B_z v_x - B_x v_z \\ (E + p^*)v_x - B_x(B_x v_x + B_y v_y + B_z v_z) \end{pmatrix}, \quad (2.7)$$

where the total pressure and the total energy are given by

$$p^* = p + \frac{1}{2}(B_x^2 + B_y^2 + B_z^2), \quad (2.8)$$

$$E = \frac{1}{2} \rho (v_x^2 + v_y^2 + v_z^2) + \frac{p}{\gamma - 1} + \frac{1}{2} (B_x^2 + B_y^2 + B_z^2). \quad (2.9)$$

With the state vector,  $\mathbf{q}$ , and the flux function,  $\mathbf{F}(\mathbf{q})$ , the Jacobian matrix,  $\mathbf{A}(\mathbf{q}) = \partial \mathbf{F} / \partial \mathbf{q}$ , is formed. The above system of equations is called “hyperbolic,” since all the eigenvalues of the Jacobian matrix are real and the corresponding set of the right eigenvectors is complete (Jeffrey & Taniuti 1964). However, the eigenvalues may coincide in some limiting cases (BW).

## 2.2. Eigenvalues and Eigenvectors for Plane-Symmetric MHD Equations

The first step to building a code based on Harten's TVD scheme (Harten 1983) for the hyperbolic system of equations shown as equation (2.5) is to get the eigenvalues and the right and left eigenvectors of the Jacobian  $A(q)$ . The seven eigenvalues in non-decreasing order are

$$a_1 = v_x - c_f, \quad (2.10)$$

$$a_2 = v_x - c_a, \quad (2.11)$$

$$a_3 = v_x - c_s, \quad (2.12)$$

$$a_4 = v_x, \quad (2.13)$$

$$a_5 = v_x + c_s, \quad (2.14)$$

$$a_6 = v_x + c_a, \quad (2.15)$$

$$a_7 = v_x + c_f, \quad (2.16)$$

where  $c_f$ ,  $c_a$ ,  $c_s$  are the fast, Alfvén, and slow characteristic speeds. The quantities  $a_1, \dots, a_7$  represent the seven speeds with which information is propagated locally by three MHD wave families and an entropy mode. The three characteristic speeds are expressed as

$$c_a = \sqrt{\frac{B_x^2}{\rho}}, \quad (2.17)$$

$$c_f = \left\{ \frac{1}{2} \left[ a^2 + \frac{B_x^2 + B_y^2 + B_z^2}{\rho} + \sqrt{\left( a^2 + \frac{B_x^2 + B_y^2 + B_z^2}{\rho} \right)^2 - 4a^2 \frac{B_x^2}{\rho}} \right] \right\}^{1/2}, \quad (2.18)$$

$$c_s = \left\{ \frac{1}{2} \left[ a^2 + \frac{B_x^2 + B_y^2 + B_z^2}{\rho} - \sqrt{\left( a^2 + \frac{B_x^2 + B_y^2 + B_z^2}{\rho} \right)^2 - 4a^2 \frac{B_x^2}{\rho}} \right] \right\}^{1/2}, \quad (2.19)$$

where  $a$  is the sound speed given by

$$a = \sqrt{\gamma \frac{p}{\rho}} \quad (2.20)$$

The corresponding right eigenvectors are (see, e.g., Jeffrey & Taniuti 1964)

$$R_{v_x \pm c_f} = \begin{pmatrix} 1 \\ v_x \pm c_f \\ v_y \mp \frac{B_x B_y c_f}{\rho(c_f^2 - c_a^2)} \\ v_z \mp \frac{B_x B_z c_f}{\rho(c_f^2 - c_a^2)} \\ \frac{B_y c_f^2}{\rho(c_f^2 - c_a^2)} \\ \frac{B_z c_f^2}{\rho(c_f^2 - c_a^2)} \\ \frac{v_x^2 + v_y^2 + v_z^2}{2} + h_f^\pm \end{pmatrix}, \quad (2.21)$$

$$R_{v_x \pm c_a} = \begin{pmatrix} 0 \\ 0 \\ \mp B_z \operatorname{sign}(B_x) \\ \pm B_y \operatorname{sign}(B_x) \\ \frac{B_z}{\sqrt{\rho}} \\ -\frac{B_y}{\sqrt{\rho}} \\ \mp (B_z v_y - B_y v_z) \operatorname{sign}(B_x) \end{pmatrix}, \quad (2.22)$$

$$R_{v_x \pm c_s} = \begin{pmatrix} 1 \\ v_x \pm c_s \\ v_y \mp \frac{B_x B_y c_s}{\rho(c_s^2 - c_a^2)} \\ \frac{B_y c_s^2}{\rho(c_s^2 - c_a^2)} \\ \frac{B_z c_s^2}{\rho(c_s^2 - c_a^2)} \\ \frac{v_x^2 + v_y^2 + v_z^2}{2} + h_s^\pm \end{pmatrix}, \quad (2.23)$$

$$R_{v_x} = \begin{pmatrix} 1 \\ v_x \\ v_y \\ v_z \\ 0 \\ 0 \\ \frac{v_x^2 + v_y^2 + v_z^2}{2} \end{pmatrix}, \quad (2.24)$$

where

$$h_f^\pm = \frac{c_f^2}{\gamma - 1} \pm c_f v_x \mp \frac{B_x c_f (B_y v_y + B_z v_z)}{\rho(c_f^2 - c_a^2)} + \frac{\gamma - 2}{\gamma - 1} (c_f^2 - a^2), \quad (2.25)$$

$$h_s^\pm = \frac{c_s^2}{\gamma - 1} \pm c_s v_x \mp \frac{B_x c_s (B_y v_y + B_z v_z)}{\rho(c_s^2 - c_a^2)} + \frac{\gamma - 2}{\gamma - 1} (c_s^2 - a^2). \quad (2.26)$$

Near the point where either  $B_x = 0$  or  $B_y = B_z = 0$ , the above set of the right eigenvectors is not well defined, with elements becoming singular. By renormalizing the eigenvectors, the singularities can be removed (BW). The renormalized eigenvectors are

$$R_{v_x \pm c_f} = \begin{pmatrix} \alpha_f \\ \alpha_f (v_x \pm c_f) \\ \alpha_f v_y \mp \alpha_s \beta_y c_a \operatorname{sign}(B_x) \\ \alpha_f v_z \mp \alpha_s \beta_z c_a \operatorname{sign}(B_x) \\ \frac{\alpha_s \beta_y c_f}{\sqrt{\rho}} \\ \frac{\alpha_s \beta_z c_f}{\sqrt{\rho}} \\ \alpha_f \frac{v_x^2 + v_y^2 + v_z^2}{2} + g_f^\pm \end{pmatrix}, \quad (2.27)$$

$$R_{v_x \pm c_a} = \begin{pmatrix} 0 \\ 0 \\ \mp \beta_z \operatorname{sign}(B_x) \\ \pm \beta_y \operatorname{sign}(B_x) \\ \frac{\beta_z}{\sqrt{\rho}} \\ -\frac{\beta_y}{\sqrt{\rho}} \\ \mp (\beta_z v_y - \beta_y v_z) \operatorname{sign}(B_x) \end{pmatrix}, \quad (2.28)$$

$$R_{v_x \pm c_s} = \begin{pmatrix} \alpha_s \\ \alpha_s(v_x \pm c_s) \\ \alpha_s v_y \pm \alpha_f \beta_y a \operatorname{sign}(B_x) \\ \alpha_s v_z \pm \alpha_f \beta_z a \operatorname{sign}(B_x) \\ -\frac{\alpha_f \beta_y a^2}{c_f \sqrt{\rho}} \\ -\frac{\alpha_f \beta_z a^2}{c_f \sqrt{\rho}} \\ \alpha_s \frac{v_x^2 + v_y^2 + v_z^2}{2} + g_s^\pm \end{pmatrix}, \quad (2.29)$$

$$R_{v_x} = \begin{pmatrix} 1 \\ v_x \\ v_y \\ v_z \\ 0 \\ 0 \\ \frac{v_x^2 + v_y^2 + v_z^2}{2} \end{pmatrix}, \quad (2.30)$$

where

$$g_f^\pm = \frac{\alpha_f c_f^2}{\gamma - 1} \pm \alpha_f c_f v_x \mp \alpha_s c_a \operatorname{sign}(B_x)(\beta_y v_y + \beta_z v_z) + \frac{\gamma - 2}{\gamma - 1} \alpha_f (c_f^2 - a^2), \quad (2.31)$$

$$g_s^\pm = \frac{\alpha_s c_s^2}{\gamma - 1} \pm \alpha_s c_s v_x \pm \alpha_f a \operatorname{sign}(B_x)(\beta_y v_y + \beta_z v_z) + \frac{\gamma - 2}{\gamma - 1} \alpha_s (c_s^2 - a^2). \quad (2.32)$$

Here  $\alpha$ 's and  $\beta$ 's are given by

$$\alpha_f = \frac{\sqrt{c_f^2 - c_a^2}}{\sqrt{c_f^2 - c_s^2}}, \quad (2.33)$$

$$\alpha_s = \frac{\sqrt{c_f^2 - a^2}}{\sqrt{c_f^2 - c_s^2}}, \quad (2.34)$$

$$\beta_y = \frac{B_y}{\sqrt{B_y^2 + B_z^2}}, \quad (2.35)$$

$$\beta_z = \frac{B_z}{\sqrt{B_y^2 + B_z^2}}. \quad (2.36)$$

At the points where  $B_y = B_z = 0$ ,  $\beta$ 's are defined as limiting values, i.e.,

$$\beta_y = \beta_z = \frac{1}{\sqrt{2}} \quad \text{if} \quad B_y = B_z = 0. \quad (2.37)$$

Similarly, at the point where  $B_y = B_z = 0$  and  $B_x^2/\rho = a^2$ ,  $\alpha$ 's are defined as

$$\alpha_f = \alpha_s = 1 \quad \text{if} \quad B_y = B_z = 0 \quad \text{and} \quad \frac{B_x^2}{\rho} = a^2. \quad (2.38)$$

Then the left eigenvectors, which are orthonormal to the right eigenvectors,  $L_l \cdot R_m = \delta_{lm}$ , are

$$L_{v_x \pm c_f} = (l_{v_x \pm c_f}^{(1)}, l_{v_x \pm c_f}^{(2)}, l_{v_x \pm c_f}^{(3)}, l_{v_x \pm c_f}^{(4)}, l_{v_x \pm c_f}^{(5)}, l_{v_x \pm c_f}^{(6)}, l_{v_x \pm c_f}^{(7)}), \quad (2.39)$$

$$l_{v_x \pm c_f}^{(1)} = \frac{1}{\theta_1} \frac{\alpha_f}{4} a^2 v^2 \mp \frac{1}{\theta_2} \left[ \frac{\alpha_f}{2} a v_x \operatorname{sign}(B_x) - \frac{\alpha_s}{2} c_s (\beta_y v_y + \beta_z v_z) \right], \quad (2.40)$$

$$l_{v_x \pm c_f}^{(2)} = -\frac{1}{\theta_1} \frac{\alpha_f}{2} a^2 v_x \pm \frac{1}{\theta_2} \frac{\alpha_f}{2} a \operatorname{sign}(B_x), \quad (2.41)$$

$$l_{v_x \pm c_f}^{(3)} = -\frac{1}{\theta_1} \frac{\alpha_f}{2} a^2 v_y \mp \frac{1}{\theta_2} \frac{\alpha_s}{2} \beta_y c_s, \quad (2.42)$$

$$l_{v_x \pm c_f}^{(4)} = -\frac{1}{\theta_1} \frac{\alpha_f}{2} a^2 v_z \mp \frac{1}{\theta_2} \frac{\alpha_s}{2} \beta_z c_s, \quad (2.43)$$

$$l_{v_x \pm c_f}^{(5)} = \frac{1}{\theta_1} \frac{\alpha_s}{2} \beta_y c_f \left( c_s^2 + \frac{2-\gamma}{\gamma-1} a^2 \right) \sqrt{\rho}, \quad (2.44)$$

$$l_{v_x \pm c_f}^{(6)} = \frac{1}{\theta_1} \frac{\alpha_s}{2} \beta_z c_f \left( c_s^2 + \frac{2-\gamma}{\gamma-1} a^2 \right) \sqrt{\rho}, \quad (2.45)$$

$$l_{v_x \pm c_f}^{(7)} = \frac{1}{\theta_1} \frac{\alpha_f}{2} a^2, \quad (2.46)$$

$$L_{v_x \pm c_a} = (l_{v_x \pm c_a}^{(1)}, l_{v_x \pm c_a}^{(2)}, l_{v_x \pm c_a}^{(3)}, l_{v_x \pm c_a}^{(4)}, l_{v_x \pm c_a}^{(5)}, l_{v_x \pm c_a}^{(6)}, l_{v_x \pm c_a}^{(7)}), \quad (2.47)$$

$$l_{v_x \pm c_a}^{(1)} = \pm \frac{\beta_z v_y - \beta_y v_z}{2} \operatorname{sign}(B_x), \quad (2.48)$$

$$l_{v_x \pm c_a}^{(2)} = 0, \quad (2.49)$$

$$l_{v_x \pm c_a}^{(3)} = \mp \frac{\beta_z}{2} \operatorname{sign}(B_x), \quad (2.50)$$

$$l_{v_x \pm c_a}^{(4)} = \pm \frac{\beta_y}{2} \operatorname{sign}(B_x), \quad (2.51)$$

$$l_{v_x \pm c_a}^{(5)} = \frac{\beta_z \sqrt{\rho}}{2}, \quad (2.52)$$

$$l_{v_x \pm c_a}^{(6)} = -\frac{\beta_y \sqrt{\rho}}{2}, \quad (2.53)$$

$$l_{v_x \pm c_a}^{(7)} = 0, \quad (2.54)$$

$$L_{v_x \pm c_s} = (l_{v_x \pm c_s}^{(1)}, l_{v_x \pm c_s}^{(2)}, l_{v_x \pm c_s}^{(3)}, l_{v_x \pm c_s}^{(4)}, l_{v_x \pm c_s}^{(5)}, l_{v_x \pm c_s}^{(6)}, l_{v_x \pm c_s}^{(7)}), \quad (2.55)$$

$$l_{v_x \pm c_s}^{(1)} = \frac{1}{\theta_1} \frac{\alpha_s}{4} c_f^2 v^2 \mp \frac{1}{\theta_2} \left[ \frac{\alpha_s}{2} c_a v_x \operatorname{sign}(B_x) + \frac{\alpha_f}{2} c_f (\beta_y v_y + \beta_z v_z) \right], \quad (2.56)$$

$$l_{v_x \pm c_s}^{(2)} = -\frac{1}{\theta_1} \frac{\alpha_s}{2} c_f^2 v_x \pm \frac{1}{\theta_2} \frac{\alpha_s}{2} c_a \operatorname{sign}(B_x), \quad (2.57)$$

$$l_{v_x \pm c_s}^{(3)} = -\frac{1}{\theta_1} \frac{\alpha_s}{2} c_f^2 v_y \pm \frac{1}{\theta_2} \frac{\alpha_f}{2} \beta_y c_f, \quad (2.58)$$

$$l_{v_x \pm c_s}^{(4)} = -\frac{1}{\theta_1} \frac{\alpha_s}{2} c_f^2 v_z \pm \frac{1}{\theta_2} \frac{\alpha_f}{2} \beta_z c_f, \quad (2.59)$$

$$l_{v_x \pm c_s}^{(5)} = -\frac{1}{\theta_1} \frac{\alpha_f}{2} \beta_y c_f \left( c_f^2 + \frac{2-\gamma}{\gamma-1} a^2 \right) \sqrt{\rho}, \quad (2.60)$$

$$l_{v_x \pm c_s}^{(6)} = -\frac{1}{\theta_1} \frac{\alpha_f}{2} \beta_z c_f \left( c_f^2 + \frac{2-\gamma}{\gamma-1} a^2 \right) \sqrt{\rho}, \quad (2.61)$$

$$l_{v_x \pm c_s}^{(7)} = \frac{1}{\theta_1} \frac{\alpha_s}{2} c_f^2, \quad (2.62)$$

$$L_{v_x} = (l_{v_x}^{(1)}, l_{v_x}^{(2)}, l_{v_x}^{(3)}, l_{v_x}^{(4)}, l_{v_x}^{(5)}, l_{v_x}^{(6)}, l_{v_x}^{(7)}), \quad (2.63)$$

$$l_{v_x}^{(1)} = 1 - \frac{1}{\theta_1} \frac{\alpha_f^2 a^2 + \alpha_s^2 c_f^2}{2} v^2, \quad (2.64)$$

$$l_{v_x}^{(2)} = \frac{1}{\theta_1} (\alpha_f^2 a^2 + \alpha_s^2 c_f^2) v_x, \quad (2.65)$$

$$l_{v_x}^{(3)} = \frac{1}{\theta_1} (\alpha_f^2 a^2 + \alpha_s^2 c_f^2) v_y, \quad (2.66)$$

$$l_{v_x}^{(4)} = \frac{1}{\theta_1} (\alpha_f^2 a^2 + \alpha_s^2 c_f^2) v_z, \quad (2.67)$$

$$l_{v_x}^{(5)} = \frac{1}{\theta_1} \alpha_f \alpha_s \beta_y c_f (c_f^2 - c_s^2) \sqrt{\rho}, \quad (2.68)$$

$$l_{v_x}^{(6)} = \frac{1}{\theta_1} \alpha_f \alpha_s \beta_z c_f (c_f^2 - c_s^2) \sqrt{\rho}, \quad (2.69)$$

$$l_{v_x}^{(7)} = -\frac{1}{\theta_1} (\alpha_f^2 a^2 + \alpha_s^2 c_f^2), \quad (2.70)$$

where

$$\theta_1 = \alpha_f^2 a^2 \left( c_f^2 + \frac{2-\gamma}{\gamma-1} a^2 \right) + \alpha_s^2 c_f^2 \left( c_s^2 + \frac{2-\gamma}{\gamma-1} a^2 \right), \quad (2.71)$$

$$\theta_2 = \alpha_f^2 c_f a \operatorname{sign}(B_x) + \alpha_s^2 c_s c_a \operatorname{sign}(B_x), \quad (2.72)$$

$$v^2 = v_x^2 + v_y^2 + v_z^2. \quad (2.73)$$

Note that, with the above normalization, some elements are not continuous functions. In order to force them to be continuous, the following term

$$\operatorname{sign}(B_T) = \begin{cases} 1, & \text{if } B_y > 0 \quad \text{or} \quad B_y = 0 \quad \text{and} \quad B_z > 0 \\ -1, & \text{if } B_y < 0 \quad \text{or} \quad B_y = 0 \quad \text{and} \quad B_z < 0, \end{cases} \quad (2.74)$$

is multiplied with  $R_{v_x \pm c_s}$  and  $L_{v_x \pm c_s}$  if  $a^2 > c_a^2$  and with  $R_{v_x \pm c_f}$  and  $L_{v_x \pm c_f}$  if  $a^2 < c_a^2$ .

It is interesting to see how the eigenvectors for the MHD equations reduce into those for the hydrodynamic equations in the limit  $B_y \rightarrow 0$  and  $B_z \rightarrow 0$ . If  $a^2 > c_a^2$ ,  $R_{v_x \pm c_f} \rightarrow R_{v_x \pm a}^{\text{HD}}$  and  $R_{v_x} \rightarrow R_{v_x}^{\text{HD}}$ , that is, the characteristics associated with MHD fast waves become those associated with hydrodynamic sound waves. The other two eigenvectors for the three-dimensional hydrodynamic equations (Roe 1981) are obtained from the following combinations of those for slow and Alfvén waves,

$$\frac{\sqrt{2} \operatorname{sign}(B_x)}{4} \left[ \frac{R_{v_x + c_s} - R_{v_x - c_s}}{a} - (R_{v_x + c_a} - R_{v_x - c_a}) \right] = \begin{pmatrix} 0 \\ 0 \\ 1 \\ 0 \\ 0 \\ 0 \\ v_y \end{pmatrix}, \quad (2.75)$$

$$\frac{\sqrt{2} \operatorname{sign}(B_x)}{4} \left[ \frac{R_{v_x + c_s} - R_{v_x - c_s}}{a} + (R_{v_x + c_a} - R_{v_x - c_a}) \right] = \begin{pmatrix} 0 \\ 0 \\ 0 \\ 1 \\ 0 \\ 0 \\ v_z \end{pmatrix}. \quad (2.76)$$

Similarly, if  $a^2 < c_a^2$ ,  $R_{v_x \pm c_s} \rightarrow R_{v_x \pm a}^{\text{HD}}$  and  $R_{v_x} \rightarrow R_{v_x}^{\text{HD}}$ , that is, the characteristics associated with MHD slow waves become those associated with hydrodynamic sound waves. The other two eigenvectors for the three-dimensional hydrodynamic equations are obtained from the following combinations of those for fast and Alfvén waves:

$$\frac{\sqrt{2} \operatorname{sign}(B_x)}{4} \left[ -\frac{R_{v_x + c_f} - R_{v_x - c_f}}{c_a} - (R_{v_x + c_a} - R_{v_x - c_a}) \right] = \begin{pmatrix} 0 \\ 0 \\ 1 \\ 0 \\ 0 \\ 0 \\ v_y \end{pmatrix}, \quad (2.77)$$

$$\frac{\sqrt{2} \operatorname{sign}(B_x)}{4} \left[ -\frac{R_{v_x+c_f} - R_{v_x-c_f}}{c_a} + (R_{v_x+c_a} - R_{v_x-c_a}) \right] = \begin{pmatrix} 0 \\ 0 \\ 0 \\ 1 \\ 0 \\ 0 \\ v_z \end{pmatrix}. \quad (2.78)$$

In cases with purely two-dimensional magnetic fields and motions (i.e.,  $B_z = v_z = 0$ ), the eigenvectors associated with Alfvén waves become

$$R_{v_x \pm c_a} = \begin{pmatrix} 0 \\ 0 \\ 0 \\ \pm \operatorname{sign}(B_x) \\ 0 \\ -\frac{1}{\sqrt{\rho}} \\ 0 \end{pmatrix}. \quad (2.79)$$

By combining them properly, they become  $(0, 0, 0, 1, 0, 0, 0)^T$  and  $(0, 0, 0, 0, 0, 1, 0)^T$ , which are trivial. This indicates that flows with two-dimensional magnetic fields do not produce structures associated with Alfvén modes like rotational discontinuities (see §§ 4 and 5 for more discussions).

### 2.3. A Second-Order Explicit TVD Scheme

Here, we describe briefly the procedure to build the MHD-TVD code with the eigenvalues and eigenvectors in the previous subsection. The purpose of this section is to provide a short but complete description of steps needed to build a code by the TVD scheme. For the details, e.g., why and how each step works, the choices for the values of internal parameters, etc., refer to the original work (Harten 1983).

The convention for indices used in this subsection is the following. The superscript  $n$  represents the time step. The subscript  $i$  indicates the quantities defined in the cell centers, while  $i + \frac{1}{2}$  identifies those defined on the cell boundaries. The subscript  $k$  represents the characteristic fields, with the order that  $k = 1$  is for the field associated with the eigenvalue  $v_x - c_f$ ,  $k = 2$  for the field with  $v_x - c_a$ ,  $k = 3$  for the field with  $v_x - c_s$ ,  $k = 4$  for the field with  $v_x$ ,  $k = 5$  for the field with  $v_x + c_s$ ,  $k = 6$  for the field with  $v_x + c_a$ , and  $k = 7$  for the field with  $v_x + c_f$ .

In a code based on the TVD scheme, the physical quantities are defined in the cell centers while the fluxes are computed on the cell boundaries. Implementation of Roe's linearization technique would result in a particular form of the averaged physical quantities on the cell boundaries (Roe 1981). However, as pointed out by BW, it is not possible to derive the analytic form of the averaged quantities in MHDs for general cases with the adiabatic index  $\gamma \neq 2$ . Instead, we should modify Roe's scheme by using the following simple averaging scheme:

$$\rho_{i+1/2} = \frac{\rho_i + \rho_{i+1}}{2}, \quad (2.80)$$

$$v_{x,i+1/2} = \frac{v_{x,i} + v_{x,i+1}}{2}, \quad (2.81)$$

$$v_{y,i+1/2} = \frac{v_{y,i} + v_{y,i+1}}{2}, \quad (2.82)$$

$$v_{z,i+1/2} = \frac{v_{z,i} + v_{z,i+1}}{2}, \quad (2.83)$$

$$B_{y,i+1/2} = \frac{B_{y,i} + B_{y,i+1}}{2}, \quad (2.84)$$

$$B_{z,i+1/2} = \frac{B_{z,i} + B_{z,i+1}}{2}, \quad (2.85)$$

$$p_{i+1/2}^* = \frac{p_i^* + p_{i+1}^*}{2}. \quad (2.86)$$



Then, other quantities like momentum, gas pressure, total energy, etc. are calculated by combining the above quantities. Our tests for cases with  $\gamma = 2$  indicated that the above simple averaging would do just as well when compared to the full implementation of Roe's linearization technique.

The state vector  $q$  at the cell center is updated by calculating the modified flux  $\bar{f}$  at the cell boundaries as follows:

$$q_i^{n+1} = q_i^n - \frac{\Delta t^n}{\Delta x} (\bar{f}_{i+1/2} - \bar{f}_{i-1/2}), \quad (2.87)$$

$$\bar{f}_{i+1/2} = \frac{1}{2} [F(q_i^n) + F(q_{i+1}^n)] - \frac{\Delta x}{2 \Delta t^n} \sum_{k=1}^7 \beta_{k,i+1/2} R_{k,i+1/2}^n, \quad (2.88)$$

$$\beta_{k,i+1/2} = Q_k \left( \frac{\Delta t^n}{\Delta x} a_{k,i+1/2}^n + \gamma_{k,i+1/2} \right) \alpha_{k,i+1/2} - (g_{k,i} + g_{k,i+1}), \quad (2.89)$$

$$\alpha_{k,i+1/2} = L_{k,i+1/2}^n \cdot (q_{i+1}^n - q_i^n), \quad (2.90)$$

$$\gamma_{k,i+1/2} = \begin{cases} \frac{g_{k,i+1} - g_{k,i}}{\alpha_{k,i+1/2}}, & \text{for } \alpha_{k,i+1/2} \neq 0, \\ 0, & \text{for } \alpha_{k,i+1/2} = 0 \end{cases}, \quad (2.91)$$

$$g_{k,i} = \text{sign}(\tilde{g}_{k,i+1/2}) \max \{0, \min [|\tilde{g}_{k,i+1/2}|, \tilde{g}_{k,i-1/2} \text{sign}(\tilde{g}_{k,i+1/2})]\}, \quad (2.92)$$

$$\tilde{g}_{k,i+1/2} = \frac{1}{2} \left[ Q_k \left( \frac{\Delta t^n}{\Delta x} a_{k,i+1/2}^n \right) - \left( \frac{\Delta t^n}{\Delta x} a_{k,i+1/2}^n \right)^2 \right] \alpha_{k,i+1/2}, \quad (2.93)$$

$$Q_k(\chi) = \begin{cases} \frac{\chi^2}{4\epsilon} + \epsilon, & \text{for } |\chi| < 2\epsilon, \\ |\chi|, & \text{for } |\chi| \geq 2\epsilon \end{cases}, \quad (2.94)$$

$$\epsilon = \begin{cases} 0.1, & \text{for } k = 1 \text{ and } 7 \\ 0.2, & \text{for } k = 2 \text{ and } 6 \\ 0.1, & \text{for } k = 3 \text{ and } 5 \\ 0.0, & \text{for } k = 4 \end{cases}. \quad (2.95)$$

Here, the time step  $\Delta t^n$  is restricted by the usual Courant condition for the stability,  $\Delta t^n = C_{\text{cour}} \Delta x / \text{Max}(|v_{x,i+1/2}^n| + c_{f,i+1/2}^n)$  with  $C_{\text{cour}} < 1$ . Typically we use  $C_{\text{cour}} = 0.8$ .

The rotational discontinuities represented by the  $k = 2$  and  $6$  fields are steepened by replacing  $g_{k,i}$  with  $g_{k,i} + \theta_{k,i} \bar{g}_{k,i}$ :

$$\theta_{k,i} = \begin{cases} \frac{|\alpha_{k,i+1/2} - \alpha_{k,i-1/2}|}{|\alpha_{k,i+1/2}| + |\alpha_{k,i-1/2}|} & \text{for } (|\alpha_{k,i+1/2}| + |\alpha_{k,i-1/2}|) \neq 0, \\ 0, & \text{for } (|\alpha_{k,i+1/2}| + |\alpha_{k,i-1/2}|) = 0 \end{cases}, \quad (2.96)$$

$$\bar{g}_{k,i} = \text{sign}(\alpha_{k,i+1/2}) \max \{0, \min [\text{sign}(\alpha_{k,i+1/2}) \sigma_{k,i-1/2} \alpha_{k,i-1/2}, \sigma_{k,i+1/2} |\alpha_{k,i+1/2}|]\}, \quad (2.97)$$

$$\sigma_{k,i+1/2} = \frac{1}{2} \left( 1 - \left| \frac{\Delta t^n}{\Delta x} a_{k,i+1/2} \right| \right). \quad (2.98)$$

With the above steepening rotational discontinuities are resolved within three to five cells; otherwise, with  $\sim 10$  cells. The contact discontinuities represented by the  $k = 4$  field could be also steepened by a similar scheme as suggested in the original TVD paper by Harten (1983). However, our tests showed that the price for steepening the contact discontinuities is additional numerical oscillations, which we deem undesirable. Thus, the tests described in § 5 do not include the steepening of the contact discontinuities by the above scheme.

### 3. A NONLINEAR MHD RIEMANN SOLVER

As a means to test quantitatively the MHD-TVD code and to understand more fully the properties of ideal MHD flows along one dimension, we developed an accurate nonlinear MHD Riemann solver. It is similar in many respects to that described in DW. The most important improvement in our MHD Riemann solver is that it treats fast and slow rarefactions properly, instead of approximating them as "rarefaction shocks" as did the solver presented in DW. We present here only essential details of the "solver," referring readers to DW for other relevant background.

As with hydrodynamic Riemann solvers, the construction of an MHD Riemann solver is based on the idea that two adjacent arbitrary states will evolve into a set of uniform states separated by left- and right-facing shocks and rarefactions. For the MHD problems, there are a total of eight states including the original pair. They are separated by six structures representing left and right propagating shocks or rarefactions of the three wave families and a structure representing the entropy mode (or the characteristic field associated with the eigenvalues  $v_x$  in the discussion of the previous section). The initial boundary moves with the structure of the entropy mode which becomes a contact discontinuity or, in degenerate cases, a tangential discontinuity (see § 4 for more

discussion). In fact, the eigenstates developed in § 2 provide approximate solutions to this problem. The particular difficulty in the MHD Riemann problem is that the equations are neither strictly hyperbolic nor strictly convex (see the discussion in BW). In practice this means that the wave speeds of two families may sometimes coincide, and that compound wave structures involving both shocks and rarefactions may sometimes develop. For the most part we can ignore this aspect and consider those situations as special cases. Otherwise we can approach the Riemann problem in pretty much the same manner as for the hydrodynamical problem, except for the larger number of waves to consider.

The solution of the problem is obtained by finding the required set of fast and slow shock jumps and rarefactions together with rotational discontinuities that self-consistently lead to a proper contact discontinuity or tangential discontinuity at the “center” of the structure. Our procedure consists of taking an initial guess for the resolved states of the (six interior) zones and then iterating toward the proper jump conditions of the contact discontinuity or the tangential discontinuity. For this discussion, the left initial state is identified with zone 1 and the right initial state is identified with zone 8. Fast structures separate zones 1 and 2 as well as zones 7 and 8. Rotational discontinuities separate zones 2 and 3 as well as zones 6 and 7. Zones 3 and 4 and zones 5 and 6 are each separated by slow structures. The contact discontinuity or the tangential discontinuity demarcates zones 4 and 5.

Discontinuities are easier to handle than rarefactions, so we outline the methods to compute discontinuities first. The problem is conceptually simpler in Lagrangian mass coordinates, where the jump conditions across a discontinuity are (e.g., eq. [2.7], DW):

$$W[V] = -[v_x], \quad (3.1)$$

$$W[v_x] = [p^* - B_x^2], \quad (3.2)$$

$$W[v_y] = -B_x[B_y], \quad (3.3)$$

$$W[v_z] = -B_x[B_z], \quad (3.4)$$

$$W[VB_y] = -B_x[v_y], \quad (3.5)$$

$$W[VB_z] = -B_x[v_z], \quad (3.6)$$

$$W[VE] = [v_x p^*] - B_x[B_x v_x + B_y v_y + B_z v_z], \quad (3.7)$$

where  $[Q] = Q_d - Q_u$  is the difference between the downstream and upstream values of a quantity  $Q$ ,  $W = -(\rho v_x)u = -(\rho v_x)_d$  is the Lagrangian speed of the discontinuity in the mass coordinates, and  $V = 1/\rho$ . The other quantities are as defined in § 2. Thus, given the upstream state and an estimate of the Lagrangian speed of the discontinuity, the downstream state can be computed.

The fast shock speed  $W_f$  and the slow shock speed  $W_s$  in the Lagrangian mass coordinates are given in DW as

$$W_{f,s}^2 = \frac{1}{2} \frac{1}{1 + S_0} [(C_s^2 + C_f^2 + S_1) \pm \sqrt{(C_s^2 + C_f^2 + S_1)^2 - 4(1 + S_0)(C_s^2 C_f^2 - S_2)}], \quad (3.8)$$

where  $C_f = \rho c_f$  and  $C_s = \rho c_s$ . The upper (lower) sign refers to fast (slow) waves. The coefficients  $S_0, S_1, S_2$  can be written in terms of the jump in tangential magnetic field across the shock,  $[B_\perp]$ , as

$$S_0 = -\frac{1}{2}(\gamma - 1) \frac{[B_\perp]}{B_\perp}, \quad (3.9)$$

$$S_1 = \frac{1}{2} \left\{ -(\gamma - 2)C_\perp^2 \frac{[B_\perp]}{B_\perp} + 2C_0^2 - (\gamma - 4)C_\perp^2 - 2\gamma C_a^2 \right\} \frac{[B_\perp]}{B_\perp}, \quad (3.10)$$

$$S_2 = \frac{1}{2} \left\{ \frac{C_a^2([B_\perp])^2}{V} + \frac{(\gamma + 2)C_\perp C_a^2[B_\perp]}{\sqrt{V}} + C_\perp^2 C_a^2(\gamma + 1) + (\gamma + 1)C_a^4 - 2C_0^2 C_a^2 \right\} \frac{[B_\perp]}{B_\perp}, \quad (3.11)$$

where  $C_0 = \rho a$  is the Lagrangian sound speed,  $C_a = \rho c_a$  is the Lagrangian Alfvén speed,  $C_\perp = B_\perp$ , and  $B_\perp = (B_y^2 + B_z^2)^{1/2}$ . All quantities except  $[B_\perp]$  in equations (3.9)–(3.11) are referred to the state upstream of the shock. The expressions used in equations (3.9)–(3.11) are equivalent to those given by DW but are somewhat simpler and in our experience have provided more robust behavior in the Riemann solver, particularly in switch-on or switch-off shocks. An expression analogous to equation (3.8) appropriate to the special case  $B_x = 0$  (magnetosonic shocks) is also given by DW. As is well known, fast and slow shocks do not alter the plane of the magnetic field.

Rotational discontinuities, which are not compressive, can be handled by setting the jump  $[v_x] = 0$  in equations (3.1) and (3.2). That leads necessarily to  $W_a = \pm C_a$ . The jump conditions required at the contact discontinuity can be found by setting  $W = 0$  in equations (3.1)–(3.7). With these results, it is clear that if the jumps of  $[B_\perp]$  across shocks and the rotations of  $[B_\perp]$  across rotational discontinuities are known then it should be possible to determine exactly the structure of any ideal MHD Riemann problem that involves only discontinuous interfaces.

DW included rarefactions in their MHD Riemann solver by assuming they could also be treated as discontinuities (i.e., as “rarefaction shocks”). So long as the rarefactions are weak this is reasonably accurate but not exact. In fact, it is also straightforward to include fast and slow rarefactions exactly, just as for hydrodynamics. By conserving all Riemann invariants through the rarefactions except that associated with the particular wave involved, one can derive a simple set of differential equations to be integrated through the rarefactions. The transitions computed in this way then replace the jumps given in equations (3.1)–(3.7).

The relations appropriate to right-facing (upper sign) and left-facing (lower sign) fast rarefactions are (e.g., Jeffrey 1966)

$$C'_0 = -\frac{\gamma+1}{2} \sqrt{\rho} \frac{C_\perp C_s^2}{C_0(C_s^2 - C_a^2)} = \frac{\gamma+1}{2} \sqrt{\rho} \frac{C_s^2(C_f^2 - C_a^2)}{C_a^2 C_\perp C_0} = \frac{\gamma+1}{2} \frac{\rho p'}{C_0}, \quad (3.12)$$

$$u'_x = \mp \frac{1}{\sqrt{\rho}} \frac{C_\perp C_a^2}{C_f(C_s^2 - C_a^2)} = \pm \frac{C_f^2 - C_a^2}{\sqrt{\rho} C_\perp C_f} = \pm \frac{2}{\gamma+1} \frac{C_0 C_a^2 C'_0}{C_s^2 C_f \rho}, \quad (3.13)$$

$$\frac{u'_y}{\cos \psi} = \frac{u'_z}{\sin \psi} = \mp \frac{1}{\sqrt{\rho}} \frac{C_a}{C_f}. \quad (3.14)$$

For right- and left-facing slow rarefactions one finds

$$C'_0 = -\frac{\gamma+1}{2} \sqrt{\rho} \frac{C_\perp C_f^2}{C_0(C_f^2 - C_a^2)} = \frac{\gamma+1}{2} \sqrt{\rho} \frac{C_f^2(C_s^2 - C_a^2)}{C_a^2 C_\perp C_0} = \frac{\gamma+1}{2} \frac{\rho p'}{C_0}, \quad (3.15)$$

$$u'_x = \mp \frac{1}{\sqrt{\rho}} \frac{C_\perp C_a^2}{C_s(C_f^2 - C_a^2)} = \pm \frac{C_s^2 - C_a^2}{\sqrt{\rho} C_\perp C_s} = \pm \frac{2}{\gamma+1} \frac{C_0 C_a^2 C'_0}{C_f^2 C_s \rho}, \quad (3.16)$$

$$\frac{u'_y}{\cos \psi} = \frac{u'_z}{\sin \psi} = \mp \frac{1}{\sqrt{\rho}} \frac{C_a}{C_s}. \quad (3.17)$$

In these expressions,  $\tan \psi = B_z/B_y$ , and primes represent derivatives with respect to  $B_\perp$ . It is also useful to have the relationship

$$(C_f^2 - C_a^2)(C_s^2 - C_a^2) = -C_a^2 C_\perp^2. \quad (3.18)$$

Our procedure for obtaining an accurate solution to a Riemann problem is similar to that employed by DW. We utilize the following steps:

1. As an initial guess, we found it convenient and mostly reliable to use the eigenvectors defined in § 2. In particular if the state vector,  $\mathbf{q}$ , defined in equation (2.6), is represented in each of the intermediate regions by  $\mathbf{q}(i)$  ( $i = 2, 3, \dots, 7$ ) then an estimate of  $\mathbf{q}(i)$  is simply

$$\mathbf{q}(i) = \mathbf{q}(8) - \sum_{k=i+1}^7 \alpha_k \mathbf{R}_k, \quad (3.19)$$

where  $\alpha_k$  is defined as in equation (2.90), and  $\mathbf{q}(8)$  is the initial right state. Occasionally the states found by equation (3.19) can have unphysical properties (i.e., jumps in  $B_\perp$  that violate eqs. [3.1]–[3.7]), so some simple physical constraints need to be applied.

2. The quantities  $B_\perp(2)$ ,  $B_\perp(4)$ ,  $B_\perp(7)$ , and  $\psi(3)$  from that solution are applied to determine jumps across each of the six waves (e.g.,  $[B_\perp]_{1 \rightarrow 2}$ ), subject to the constraints that  $B_\perp(5) = B_\perp(4)$  and  $\psi(4-6) = \psi(3)$ . This is accomplished by starting with the two fast waves, followed by the two rotations of  $B_\perp$  and finally the two slow waves.

3. For the solution to be considered exact, we require that the resulting jump conditions at the contact discontinuity precisely satisfy those expected from equations (3.1)–(3.7). In particular, we test if all the jumps  $[v_x]$ ,  $[v_y]$ ,  $[v_z]$ , and  $[p^*] = 0$ .

4. If the contact discontinuity jump conditions are not satisfied, we vary  $B_\perp(2)$ ,  $B_\perp(4)$ ,  $B_\perp(7)$ , and  $\psi(3)$  using a Newton-Raphson scheme based on a numerical approximation to the associated Jacobian matrix for an improved guess in the quantities  $B_\perp(2)$ ,  $B_\perp(4)$ ,  $B_\perp(7)$ , and  $\psi(3)$ .

5. The procedure, beginning with step (2), is then repeated until convergence is obtained. The accuracy of the initial guess is the single most important aspect controlling the number of iterations required. Once a reasonably approximate solution is found, usually only a couple of iterations lead to very good convergence.

When  $B_x = 0$ , the same scheme is applied, but in somewhat simplified form, since there are no slow wave features or rotational discontinuities, and the constraint  $\psi(4) = \psi(5)$  is removed.

With these procedures, we are able in most cases to obtain solutions such that the contact discontinuity jump conditions are very well satisfied, even to near the limits of machine accuracy. In practice, we establish a convergence criterion of  $10^{-6}$  relative to the larger of a zone-averaged  $v_x$  or fast wave speed for velocities or total pressure for  $[p^*]$ . Only for Riemann problems involving switch-off or switch-on waves are we significantly limited, since an exact switch-on or switch-off feature requires either the upstream or downstream flow speed to exactly equal the Alfvén speed. In those cases, even very small errors in  $[B_\perp]$  lead to significant errors in  $W$ , and so the remaining downstream state variables. We found that we could obtain precise solutions only if we permitted the smaller  $B_\perp$  next to such a wave to have a value  $\sim 10^{-3}$  of the larger  $B_\perp$ . These waves are for almost any practical purpose indistinguishable from exact switch waves, however.

We will discuss tests of the Riemann solver along with the tests of the MHD-TVD code in the next section, since we test them against each other in many cases. Suffice it to say here that, to start with, we examined our Riemann solver against all those solutions presented in DW and against a number of other examples kindly given to us by W. Dai which were also generated with the Riemann solver described in DW. In the cases involving only discontinuities, our solutions agree exactly with the DW results. When there are rarefactions, we find some, mostly minor ( $\lesssim 1\%$ ) differences. But those are attributable to the fact that we treated

rarefactions exactly, whereas they did not. The differences are so small, however, that the only really practical limitation of the DW Riemann solver is that it cannot determine the structure of rarefactions. For use to determine intermediate states in a numerical code it is quite adequate.

#### 4. NUMERICAL TESTS

To test the MHD-TVD code described in § 2 as well as the Riemann solver described in § 3, we chose MHD shock tube problems including those considered in BW and DW. In all the tests, we set the adiabatic index  $\gamma = 5/3$  and used a one-dimensional box with  $x = [0, 1]$ . The numerical calculations were done with a Courant constant 0.8, with steepening of the rotational discontinuity, but without steepening of the contact discontinuity. The results of the numerical calculations with the code are plotted as dots, and the analytic solutions of the nonlinear Riemann solver are plotted as lines. The plotted quantities are density, gas pressure, total (thermal, kinetic, and magnetic) energy,  $x$ -velocity (parallel to the direction of structure propagation),  $y$ -velocity,  $z$ -velocity,  $y$ -magnetic field,  $z$ -magnetic field, and the orientation angle of tangential magnetic field [ $\psi = \tan^{-1}(B_z/B_y)$ ] in the plane perpendicular to the propagation vector. Numerical values of the analytic solutions in the regions between the structures (e.g., between the left-moving fast shock and the left-moving rotational discontinuity, etc.) are listed in Tables 1–5 with the same labels as the figures. To simplify the discussion of this section we refer to solutions as “two-dimensional” when the magnetic field remains in one plane through the entire structure, or “three-dimensional” when the field cannot be so described.

The first set of tests (also found in DW) has been done with two-dimensional field and velocity structure in the  $x$ - $y$  plane but without change in the direction of the tangential magnetic field ( $B_y$  in these tests). Figure 1a shows the solution of the MHD shock tube test with the left state  $(\rho, v_x, v_y, v_z, B_y, B_z, E) = [1, 10, 0, 0, 5/(4\pi)^{1/2}, 0, 20]$  and the right state  $[1, -10, 0, 0, 5/(4\pi)^{1/2}, 0, 1]$  with  $B_x = 5/(4\pi)^{1/2}$  at time  $t = 0.08$ . The plot shows a pair of fast shocks, a left-facing slow rarefaction, a right-facing slow shock, and a contact discontinuity.

Figure 1b shows the solution of the MHD shock tube test with the left state  $(\rho, v_x, v_y, v_z, B_y, B_z, E) = [1, 0, 0, 0, 5/(4\pi)^{1/2}, 0, 1]$  and the right state  $[0.1, 0, 0, 0, 2/(4\pi)^{1/2}, 0, 10]$  with  $B_x = 3/(4\pi)^{1/2}$  at time  $t = 0.03$ . The plot shows one fast shock and one fast rarefaction, one slow shock and one slow rarefaction, and a contact discontinuity. As expected from the two-dimensional nature of the field and velocity structure, there is no rotational discontinuity in either of these flows. In the numerical calculations, fast shocks that are strong with a large parallel velocity jump,  $[v_x]$ , are resolved within two to four cells. However, slow shocks that are weak with a small velocity jump can require from 10 to 20 cells to be resolved, with the number of cells being greater for weaker shocks. Contact discontinuities typically spread over  $\sim 10$  cells. In Figure 1b, the density found by the numerical calculation is slightly smaller than that found by the Riemann solver between the left-moving slow shock and the contact discontinuity. That difference is a temporary feature of the simulation and comes from the fact that at the time shown only about two cells separate the positions of the shock and contact discontinuity. That is not adequate to capture the full amplitude of the structure.

The second set of tests involves three-dimensional field and velocity structure where the magnetic field plane rotates. The solution of the MHD shock tube test with the left state  $(\rho, v_x, v_y, v_z, B_y, B_z, E) = [1.08, 1.2, 0.01, 0.5, 3.6/(4\pi)^{1/2}, 2/(4\pi)^{1/2}, 0.95]$  and the right state  $[1, 0, 0, 0, 4/(4\pi)^{1/2}, 2/(4\pi)^{1/2}, 1]$  with  $B_x = 2/(4\pi)^{1/2}$  at time  $t = 0.2$  is plotted in Figure 2a. DW also provide the Riemann solution for this test. Fast shocks, rotational discontinuities, and slow shocks propagate from each side of the contact discontinuity.

The solution of the MHD shock tube test with the left state  $(\rho, v_x, v_y, v_z, B_y, B_z, E) = [1, 0, 0, 0, 6/(4\pi)^{1/2}, 0, 1]$  and the right state  $[0.1, 0, 2, 1, 1/(4\pi)^{1/2}, 0, 10]$  with  $B_x = 3/(4\pi)^{1/2}$  at time  $t = 0.035$  is plotted in Figure 2b. A fast shock, a rotational discontinuity, and a slow shock propagate from the left side of the contact discontinuity, while a fast rarefaction, a rotational discontinuity, and a slow rarefaction propagate to the right. The rotation across the initial discontinuity of the magnetic field generates two rotational discontinuities. As in the previous case, strong fast shocks are resolved within two to four cells, but weak slow shocks take more cells. With “proper” steepening (meaning steepening that does not generate oscillations), the rotational discontinuities spread over only three to five cells, but without steepening the contact discontinuities spread over more cells. In Figure 2b, the numerical calculation produces smaller density between the left-moving slow shock and the contact discontinuity and smaller  $v_z$  and  $B_z$  between the left rotational discontinuity and the left-moving slow shock compared to the Riemann solution. In addition there is a slight error in the angle  $\psi$  between these discontinuities. Again, these are temporary properties of the solution resulting from the fact that the waves involved are propagating at almost the same speed and have not had time to separate more than a couple of cells. At the same time it is clear that the MHD-TVD code has captured the presence of all of the discontinuities even though they are very close together. With the right rotational discontinuity located very close to the right-moving slow rarefaction wave at this time, the code has smoothed the foot of the right-facing slow rarefaction noticeably in  $v_z$  and  $B_z$ .

The third test set demonstrates handling of magnetosonic structures with vanishing tangential flow velocity and parallel magnetic field. A test from DW for magnetosonic shocks is set up with the left state  $(\rho, v_x, v_y, v_z, B_y, B_z, E) = [0.1, 50, 0, 0, -1/(4\pi)^{1/2}, -2/(4\pi)^{1/2}, 0.4]$  and the right state  $[0.1, 0, 0, 0, 1/(4\pi)^{1/2}, 2/(4\pi)^{1/2}, 0.2]$  and with  $B_x = 0$ . The solution has a pair of magnetosonic shocks propagating from a tangential discontinuity and is plotted at time  $t = 0.01$  in Figure 3a. Magnetosonic shocks are fast shocks with zero parallel field ( $B_x = 0$ ) and they are resolved within two to four cells like fast shocks. The tangential discontinuity, which is a degenerate combination of one contact discontinuity, two slow structures, and two rotational discontinuities, spreads over  $\sim 15$  cells. Even with the steepening described in § 2, we could not prevent the spreading of the tangential discontinuity in numerical calculations. There is a small “glitch” associated with the tangential discontinuity visible for both the density and gas pressure. Such features are commonly formed at contact discontinuities in shock tube simulations involving separating strong shock pairs, even in gasdynamic calculations with such robust schemes as “PPM.”

The test for magnetosonic rarefactions are set up with the left state  $(\rho, v_x, v_y, v_z, B_y, B_z, E) = (1, -1, 0, 0, 1, 0, 1)$  and the right state  $(1, 1, 0, 0, 1, 0, 1)$  and with  $B_x = 0$ . The solution has only two strong and identical magnetosonic rarefactions and is plotted at time  $t = 0.1$  in Figure 3b. Again, small errors in density and gas pressure are visible at the position of the tangential discontinuity. And, as before, we note that such errors are common to shock tube simulations involving strong rarefactions.



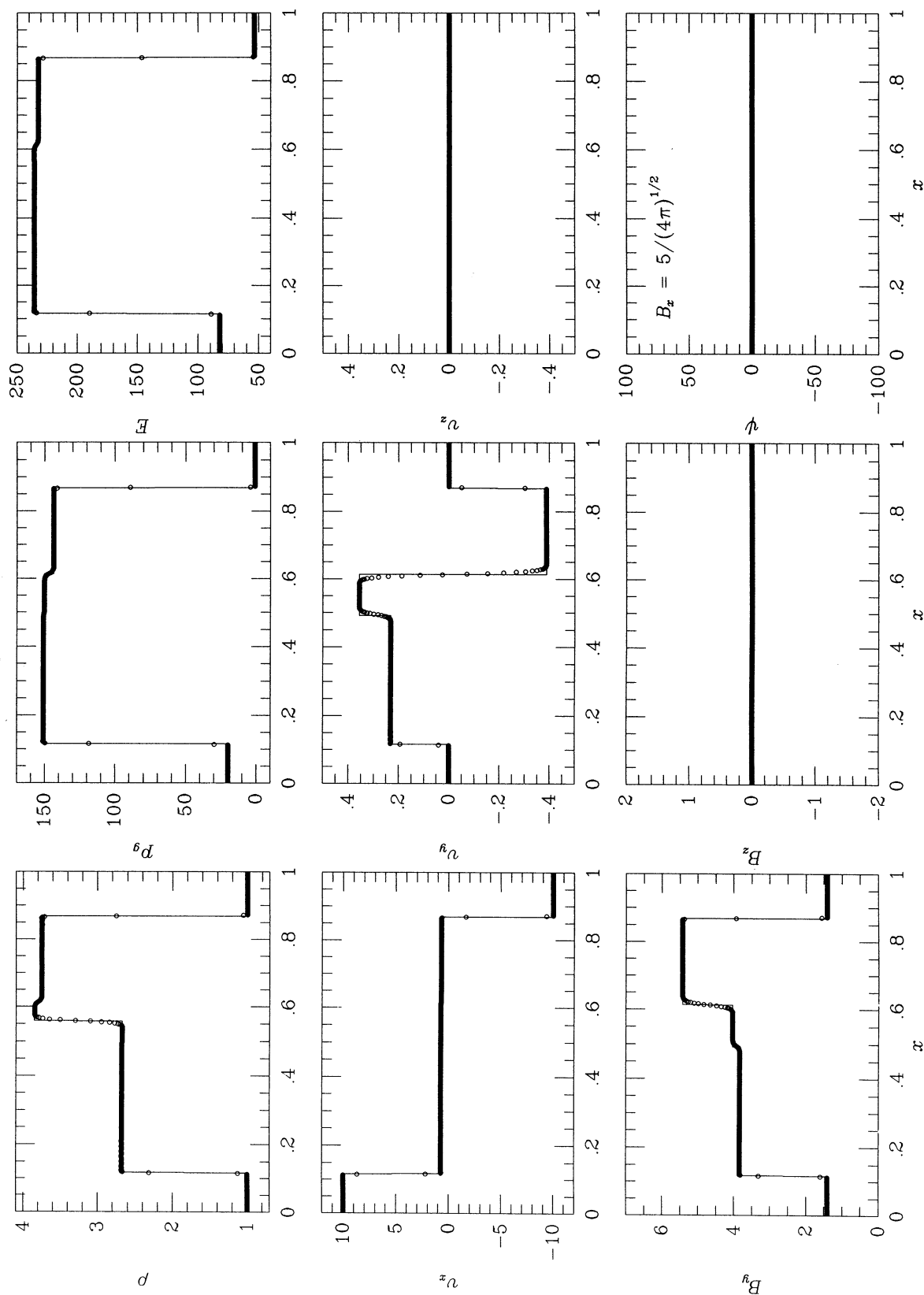


FIG. 1a.—Solution of the MHD shock tube test with the left state  $(\rho, v_x, v_y, v_z, B_x, B_y, E) = [1, 10, 0, 0, 5/(4\pi)^{1/2}, 0, 20]$  and the right state  $[1, -10, 0, 0, 5/(4\pi)^{1/2}, 0, 1]$  with  $B_x = 5/(4\pi)^{1/2}$  and  $\gamma = 5/3$  at time  $t = 0.08$  (test in DW, Table 6). Dots are the result of a numerical calculation with the MHD-TVD code described in § 2 using 512 cells and a Courant constant of 0.8. Lines are the result with the nonlinear Riemann solver described in § 3. Plots show from left to right (1) fast shock, (2) slow rarefaction, (3) contact discontinuity, (4) slow shock, and (5) fast shock.

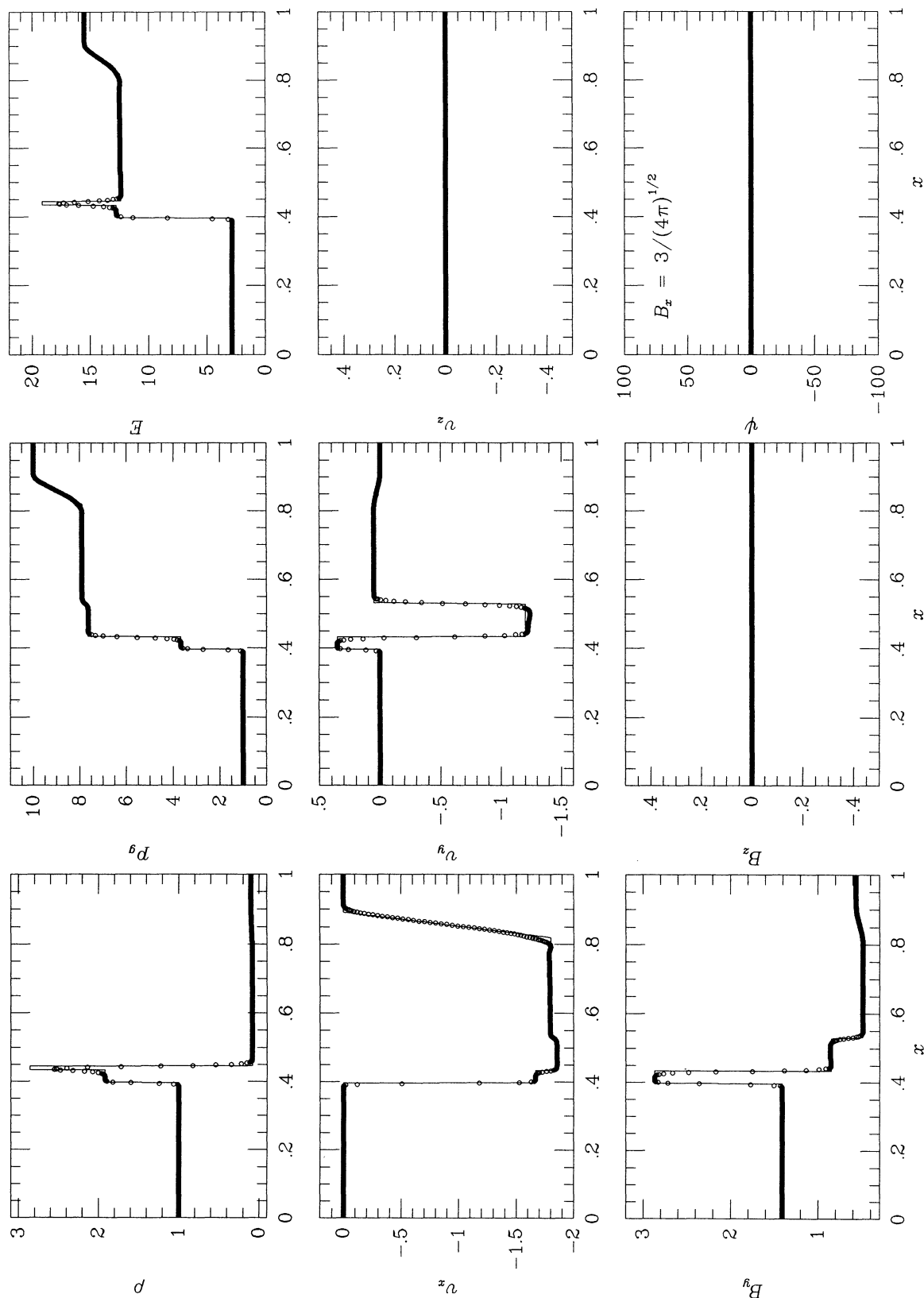


FIG. 1b.—Solution of the MHD shock tube test with the left state  $(\rho, v_x, v_y, v_z, B_x, B_y, B_z, E) = [1, 0, 0, 0, 5/(4\pi)^{1/2}, 0, 1]$  and the right state  $[0.1, 0, 0, 2/(4\pi)^{1/2}, 0, 10]$  with  $B_x = 3/(4\pi)^{1/2}$  and  $\gamma = 5/3$  at time  $t = 0.03$  (test in DW Table 3A). Dots are the result of a numerical calculation with the MHD-TVD code described in § 2 using 512 cells and a Courant constant of 0.8. Lines are the result with the nonlinear Riemann solver described in § 3. Plots show from left to right (1) fast shock, (2) slow shock, (3) contact discontinuity, (4) slow rarefaction, and (5) fast rarefaction.

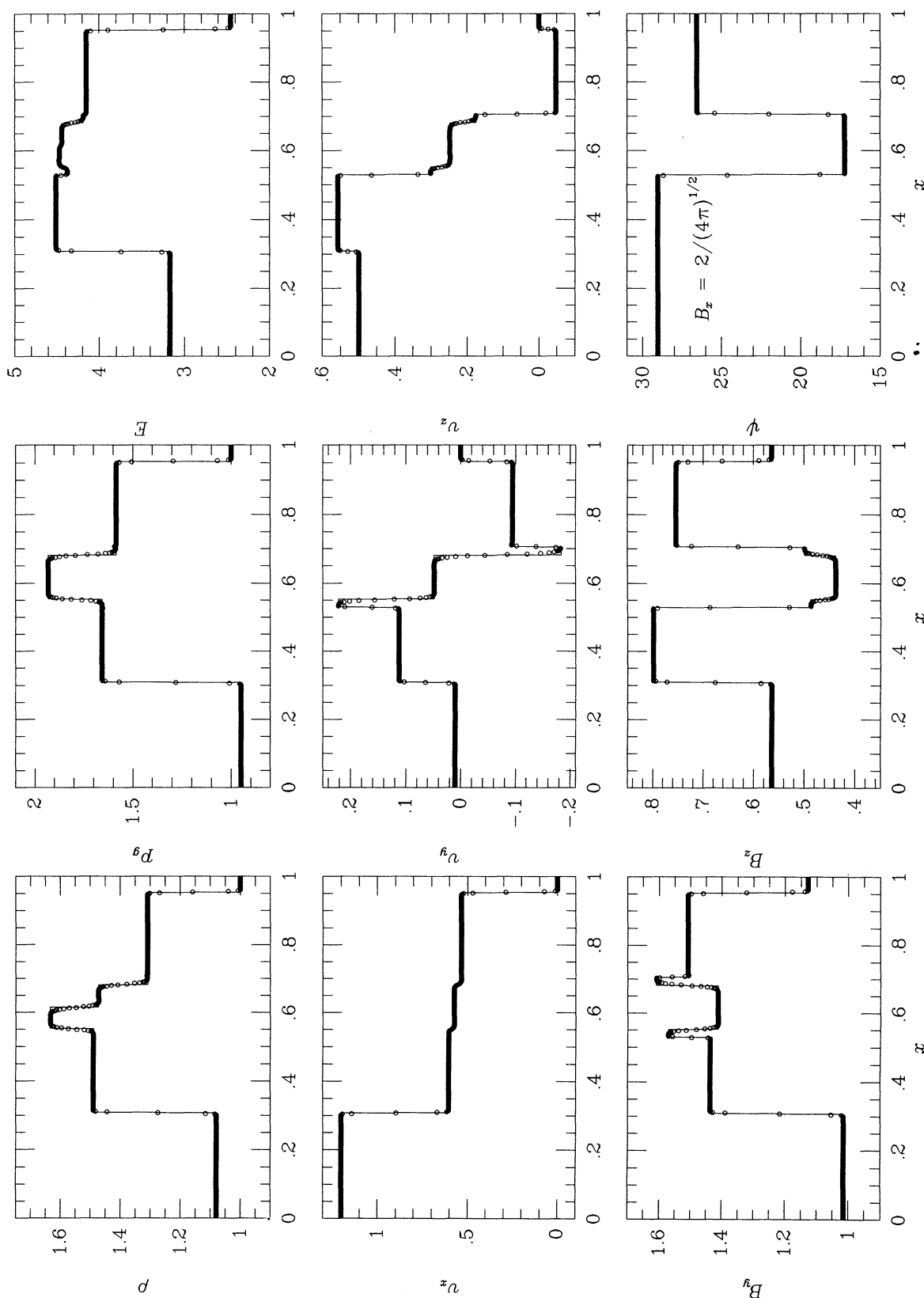


FIG. 2a—Solution of the MHD shock tube test with the left state  $(\rho, v_x, v_y, v_z, B_x, B_y, B_z, E) = [1.08, 1.2, 0.01, 0.5, 3.6/(4\pi)^{1/2}, 2/(4\pi)^{1/2}, 2/(4\pi)^{1/2}, 1]$  with  $B_x = 2/(4\pi)^{1/2}$  and  $\gamma = 5/3$  at time  $t = 0.2$  (test in DW, Table 1A). Dots are the result of a numerical calculation with the MHD-TVD code described in § 2 using 512 cells and a Courant constant of 0.8. Lines are the result with the nonlinear Riemann solver described in § 3. Plots show from left to right (1) fast shock, (2) rotational discontinuity, (3) slow shock, (4) contact discontinuity, (5) slow shock, (6) rotational discontinuity, and (7) fast shock.

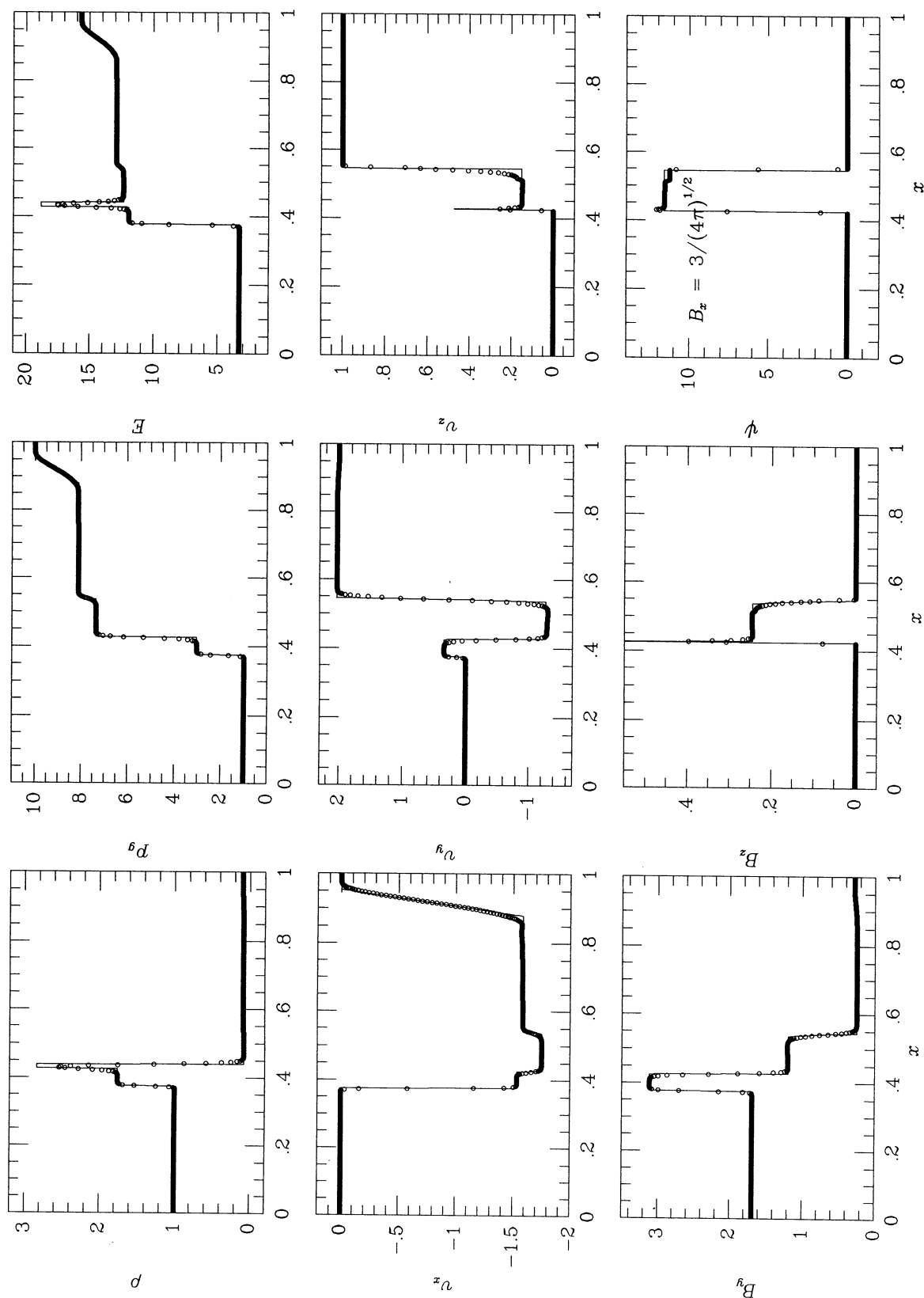


FIG. 2b.—Solution of the MHD shock tube test with the left state  $(\rho, v_x, v_y, v_z, B_x, B_y, B_z, E) = [1, 0, 0, 0, 6/(4\pi)^{1/2}, 0, 1]$  and the right state  $[0.1, 0, 2, 1, 1/(4\pi)^{1/2}, 0, 10]$  with  $B_x = 3/(4\pi)^{1/2}$  and  $\gamma = 5/3$  at time  $t = 0.035$ . Dots are the result of a numerical calculation with the MHD-TVD code described in § 2 using 512 cells and a Courant constant of 0.8. Lines are the result with the nonlinear Riemann solver described in § 3. Plots show from left to right (1) fast shock, (2) rotational discontinuity, (3) slow shock, (4) contact discontinuity, (5) slow rarefaction, (6) rotational discontinuity, and (7) fast rarefaction.



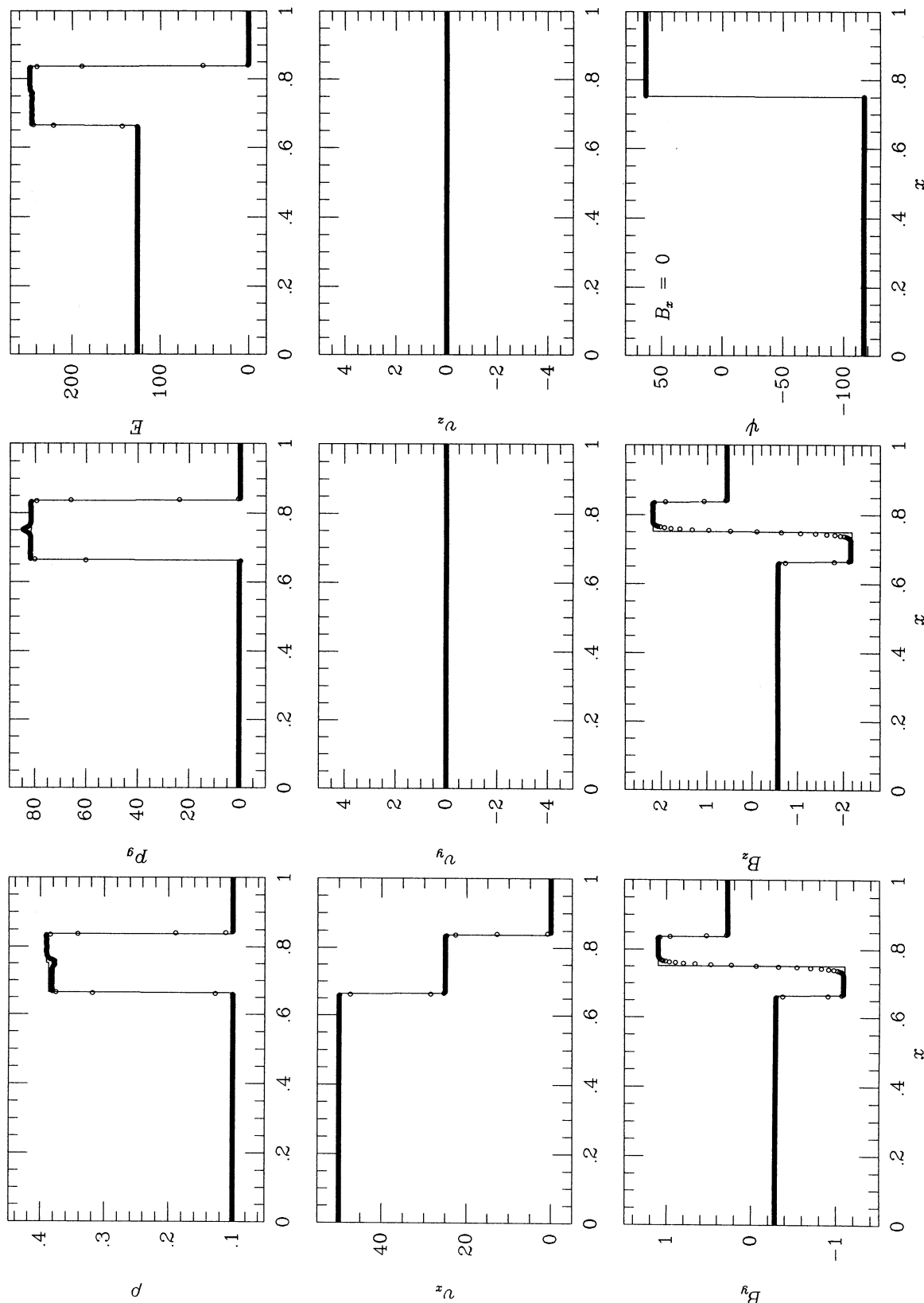
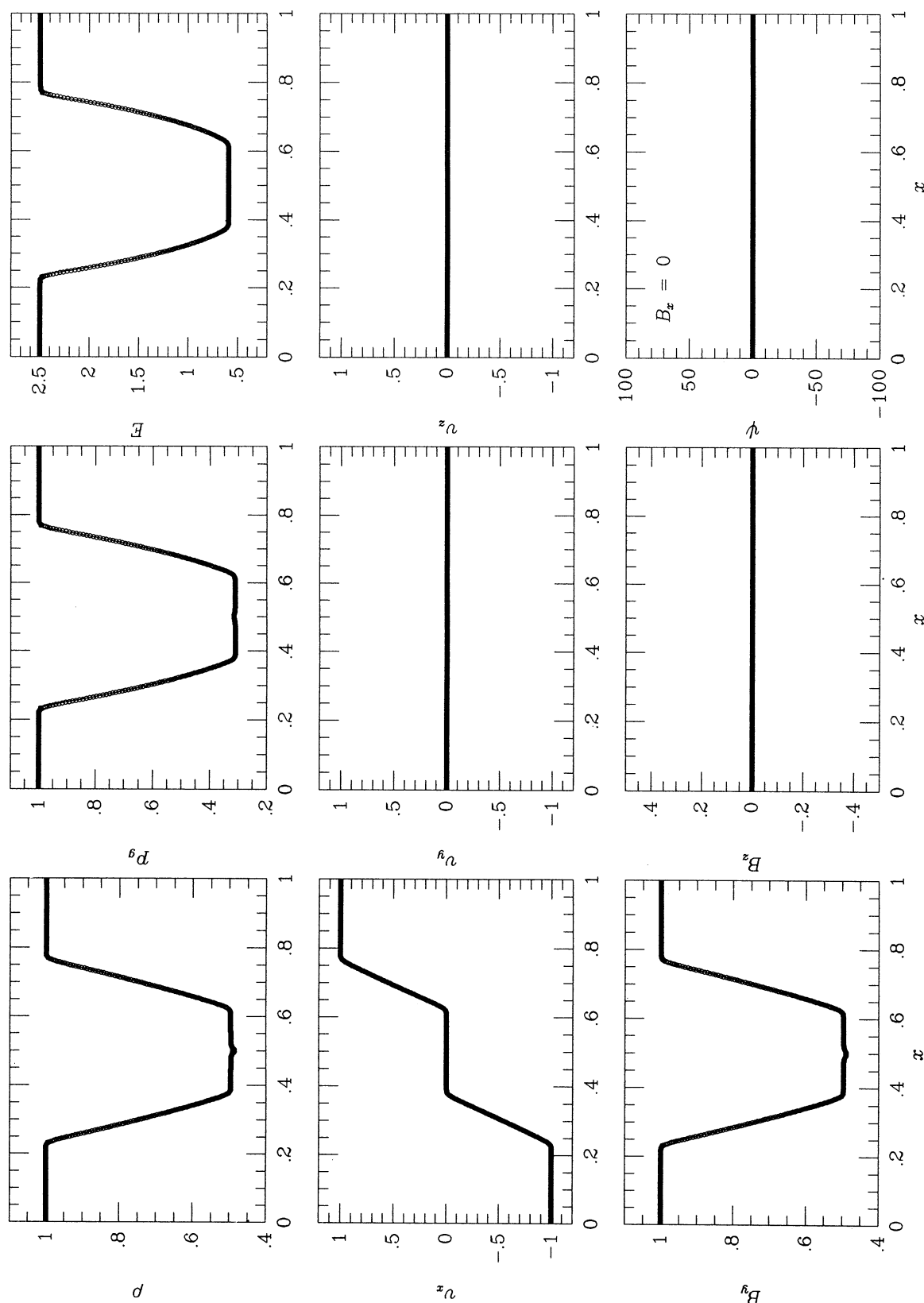


Fig. 3a.—Solution of the MHD shock tube test with the left state  $(\rho, v_x, v_y, v_z, B_x, B_y, B_z, E) = [0.1, 50, 0, 0, -1/(4\pi)^{1/2}, -2/(4\pi)^{1/2}, 2/(4\pi)^{1/2}, 0.2]$  with  $B_x = 0$  and  $\gamma = 5/3$  at time  $t = 0.01$  (test in DW, Table 2A). Dots are the result of a numerical calculation with the MHD-TVD code described in § 2 using 512 cells and a Courant constant of 0.8. Lines are the result with the nonlinear Riemann solver described in § 3. Plots show from left to right (1) magnetosonic shock, (2) tangential discontinuity, and (3) magnetosonic shock.



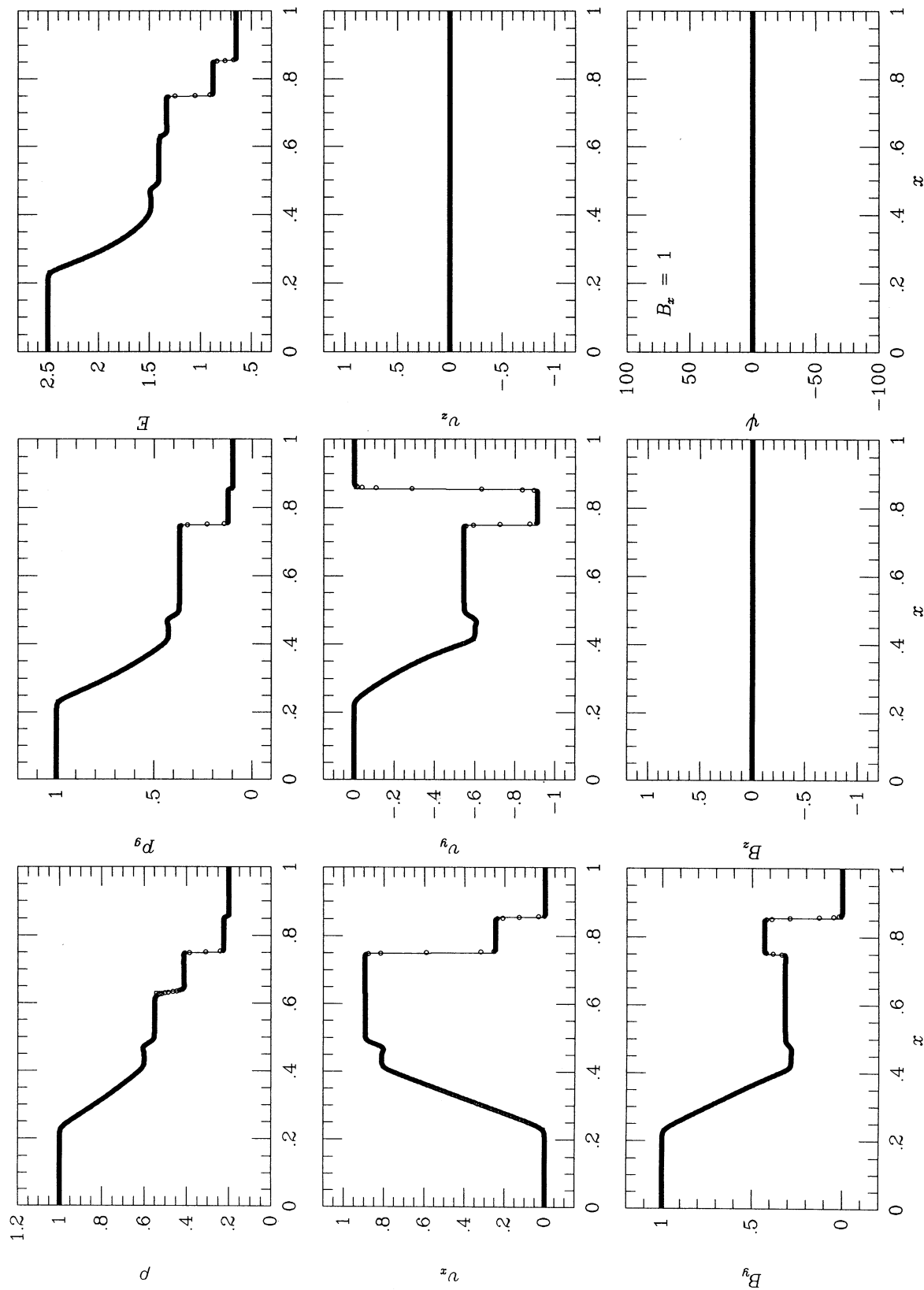


FIG. 4a.—Solution of the MHD shock tube test with the left state  $(\rho, v_x, v_y, v_z, B_x, B_y, B_z, E) = (1, 0, 0, 0, 1, 0, 1)$  and the right state  $(0.2, 0, 0, 0, 0, 0, 0.1)$  with  $B_x = 1$  and  $\gamma = 5/3$  at time  $t = 0.15$ . Dots are the result of a numerical calculation with the MHD-TVD code described in § 2 using 512 cells and a Courant constant of 0.8. Lines are the result with the nonlinear Riemann solver described in § 3. Plots show from left to right (1) fast rarefaction, (2) slow rarefaction, (3) contact discontinuity, (4) slow shock, and (5) switch-on fast shock.

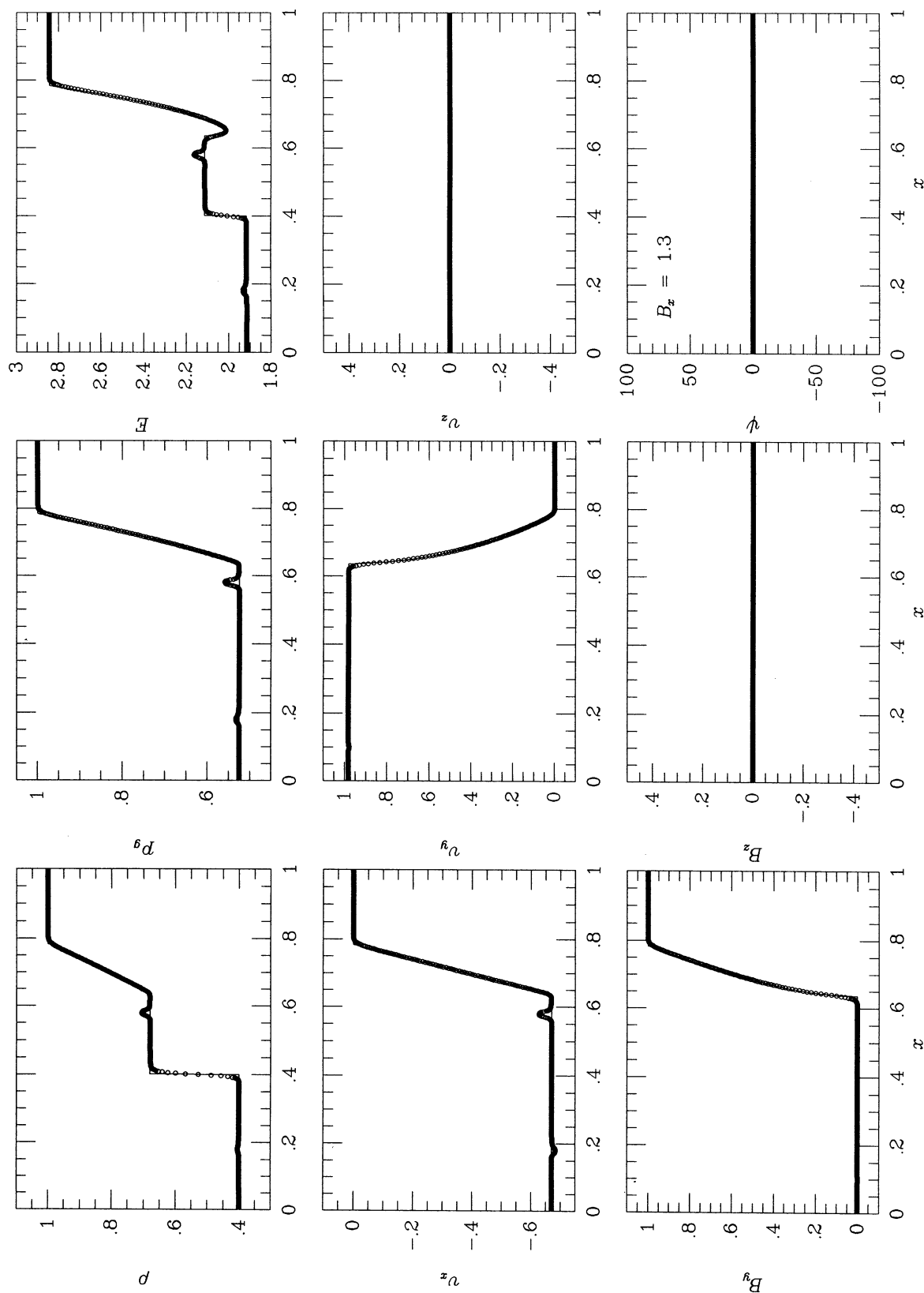


FIG. 4b.—Solution of the MHD shock tube test with the left state  $(\rho, v_x, v_y, v_z, B_x, B_y, B_z, E) = (0.4, -0.66991, 0.98263, 0, 0.0025293, 0, 0.52467)$  and the right state  $(1, 0, 0, 0, 1, 0, 1)$  with  $B_x = 1.3$  and  $\gamma = 5/3$  at time  $t = 0.15$ . Dots are the result of a numerical calculation with the MHD-TVD code described in § 2 using 512 cells and a Courant constant of 0.8. Lines are the result with the nonlinear Riemann solver described in § 3. Plots show from left to right (1) contact discontinuity and (2) switch-off fast rarefaction.

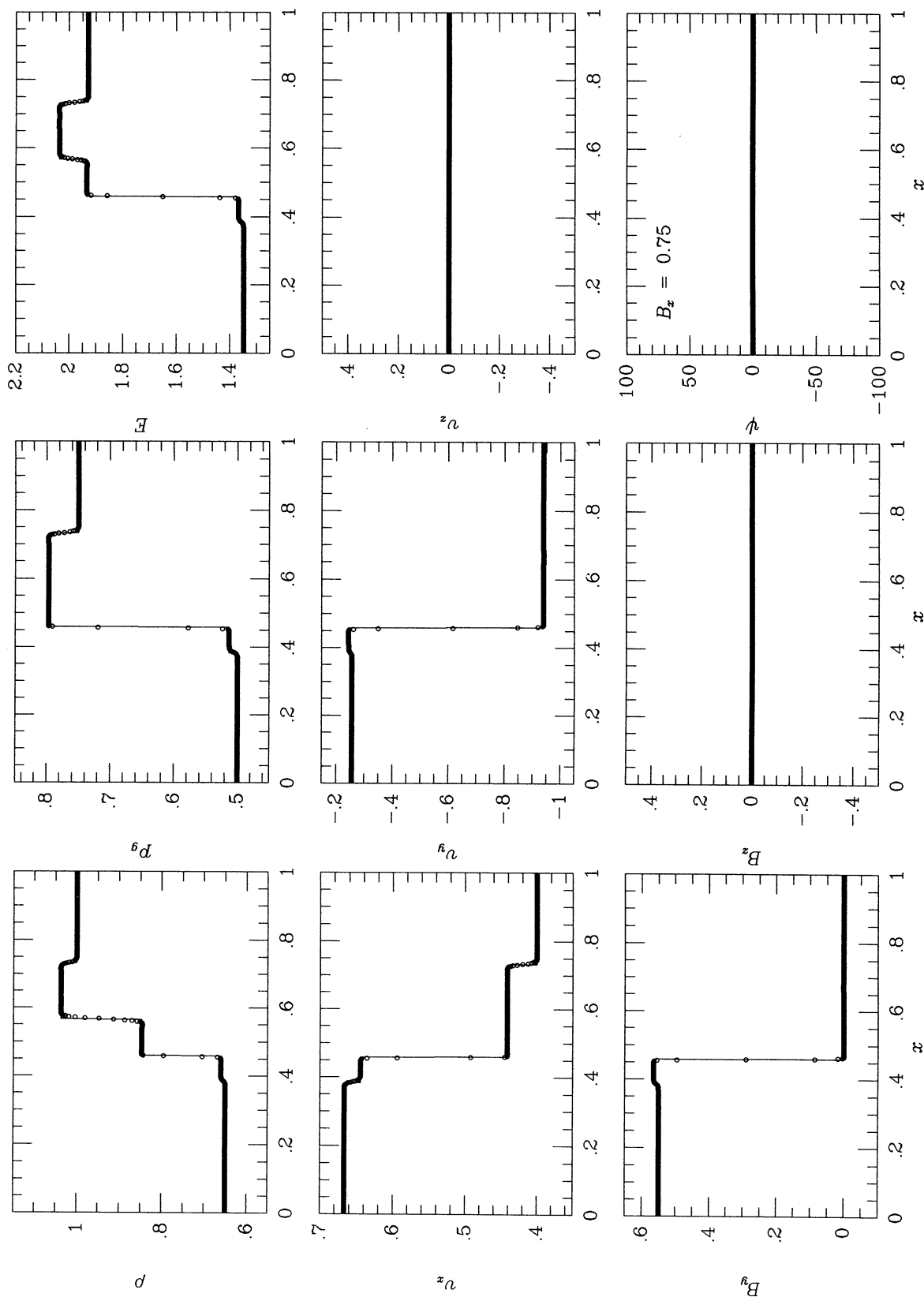


FIG. 4c.—Solution of the MHD shock tube test with the left state  $(\rho, v_x, v_y, v_z, B_x, B_y, B_z, E) = (0.65, 0.667, -0.257, 0, 0.55, 0, 0.5)$  and the right state  $(1, 0.4, -0.94, 0, 0, 0.75)$  with  $B_x = 0.75$  and  $\gamma = 5/3$  at time  $t = 0.15$ . Dots are the result of a numerical calculation with the MHD-TVD code described in § 2 using 512 cells and a Courant constant of 0.8. Lines are the result with the nonlinear Riemann solver described in § 3. Plots show from left to right (1) fast shock, (2) switch-off slow shock, (3) contact discontinuity, and (4) hydrodynamic shock.

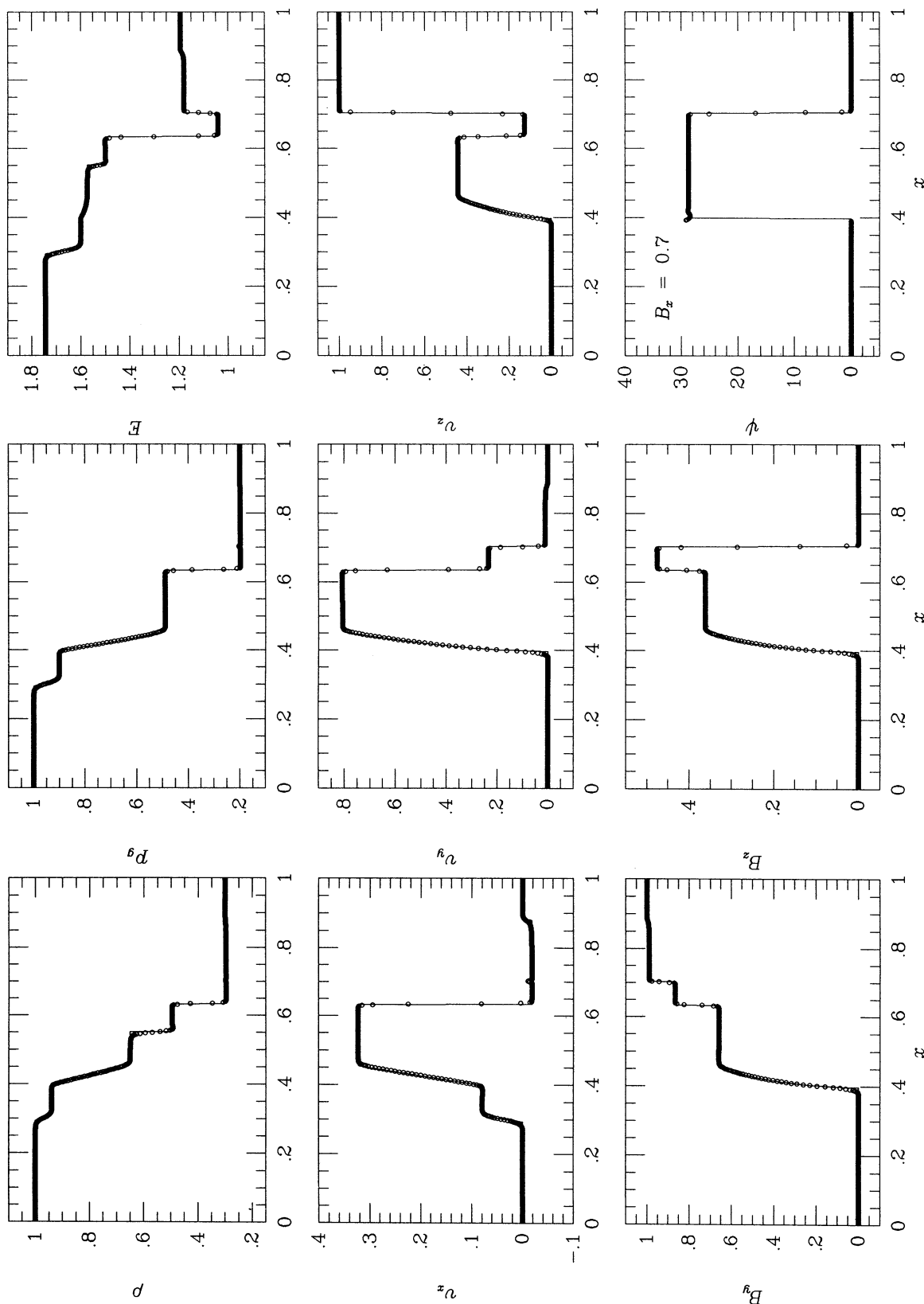


FIG. 4d.—Solution of the MHD shock tube test with the left state  $(\rho, v_x, v_y, v_z, B_x, B_y, B_z, E) = (1, 0, 0, 0, 0, 1)$  and the right state  $(0.3, 0, 0, 1, 1, 0, 0.2)$  with  $B_x = 0.7$  and  $\gamma = 5/3$  at time  $t = 0.16$ . Dots are the result of a numerical calculation with the MHD-TVD code described in § 2 using 512 cells and a Courant constant of 0.8. Lines are the result with the nonlinear Riemann solver described in § 3. Plots show from left to right (1) hydrodynamic rarefaction, (2) switch-on slow rarefaction, (3) contact discontinuity, (4) slow shock, (5) rotational discontinuity, and (6) fast rarefaction.

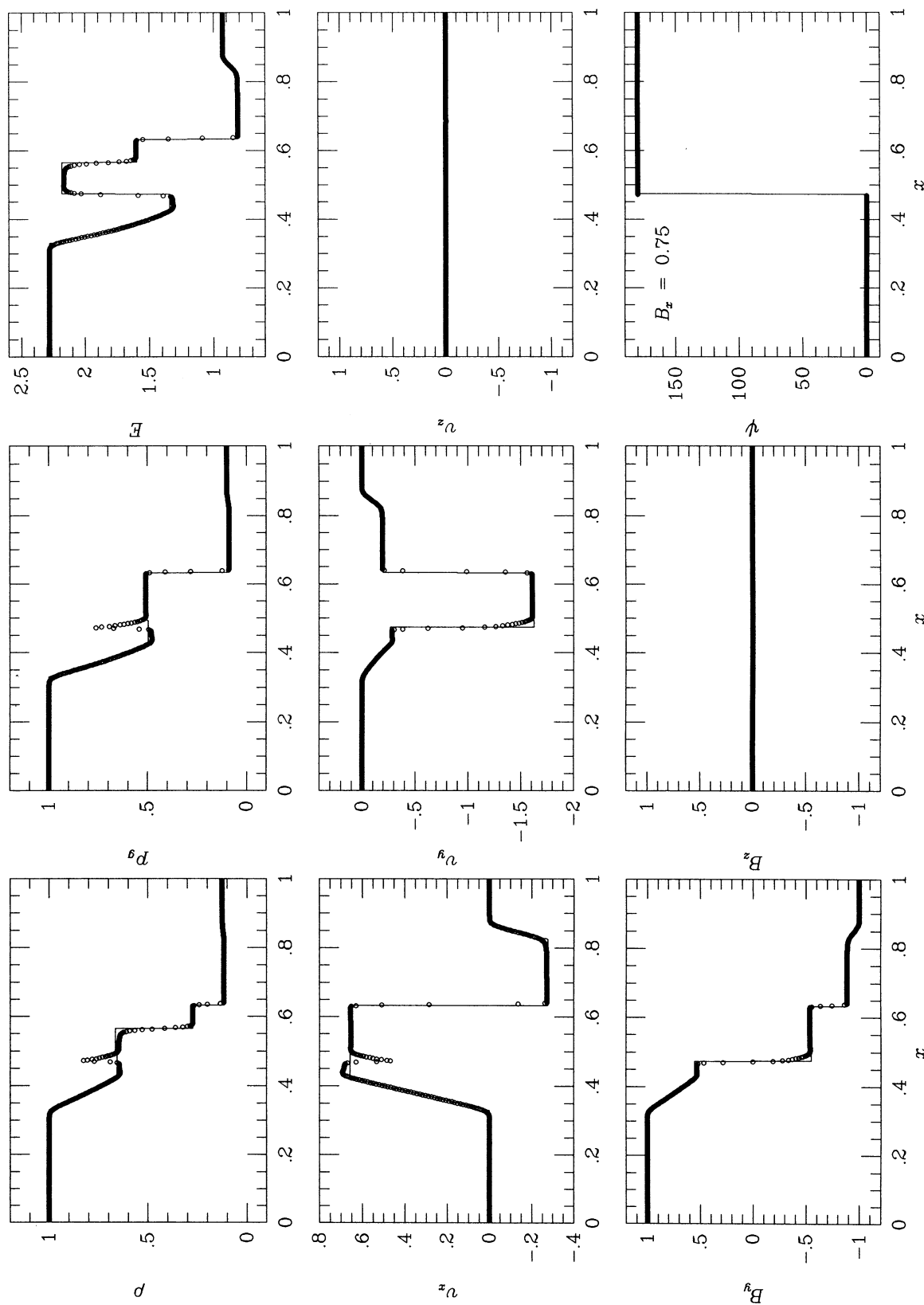


FIG. 5a.—Solution of the MHD shock tube test with the left state  $(\rho, v_x, v_y, v_z, B_x, B_y, B_z, E) = (1, 0, 0, 0, 1, 0, 1)$  and the right state  $(0.125, 0, 0, 0, -1, 0, 0.1)$  with  $B_x = 0.75$  and  $\gamma = 5/3$  at time  $t = 0.1$  (test in BW). Dots are the result of a numerical calculation with the MHD-TVD code described in § 2 using 512 cells and a Courant constant of 0.8. Lines are the result with the nonlinear Riemann solver described in § 3. Plots show from left to right (1) fast rarefaction, (2) slow rarefaction, (3) contact discontinuity, (4) slow shock, and (5) fast rarefaction.

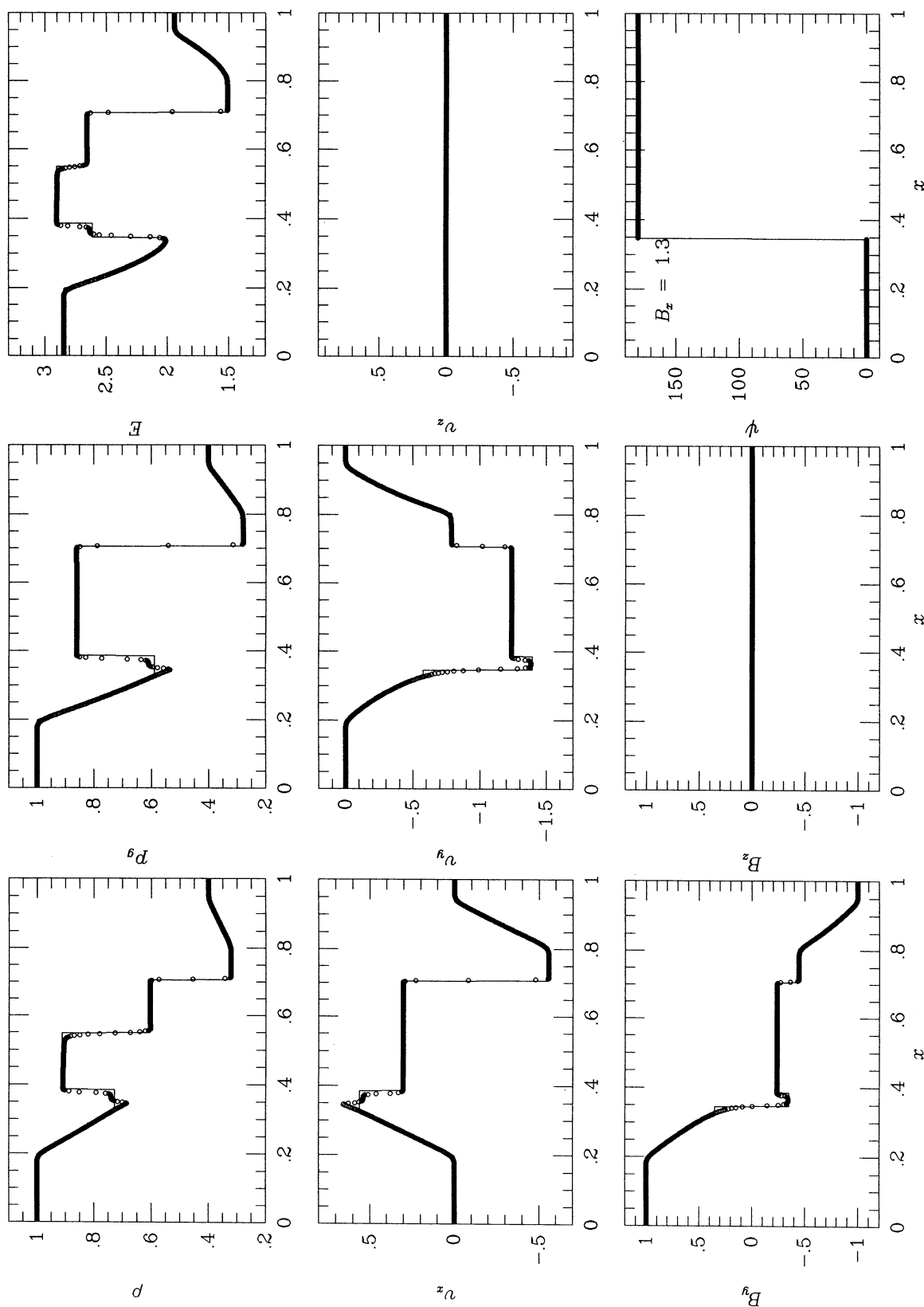


FIG. 5b.—Solution of the MHD shock tube test with the left state  $(\rho, v_x, v_y, v_z, B_x, B_y, B_z, E) = (1, 0, 0, 0, 1, 0, 1)$  and the right state  $(0.4, 0, 0, 0, -1, 0, 0.4)$  with  $B_x = 1.3$  and  $\gamma = 5/3$  at time  $t = 0.16$ . Dots are the result of a numerical calculation with the MHD-TVD code described in § 2 using 512 cells and a Courant constant of 0.8. Lines are the result with the nonlinear Riemann solver described in § 3. Plots show from left to right (1) fast compound, (2) slow shock, (3) contact discontinuity, (4) slow shock, and (5) fast rarefaction.



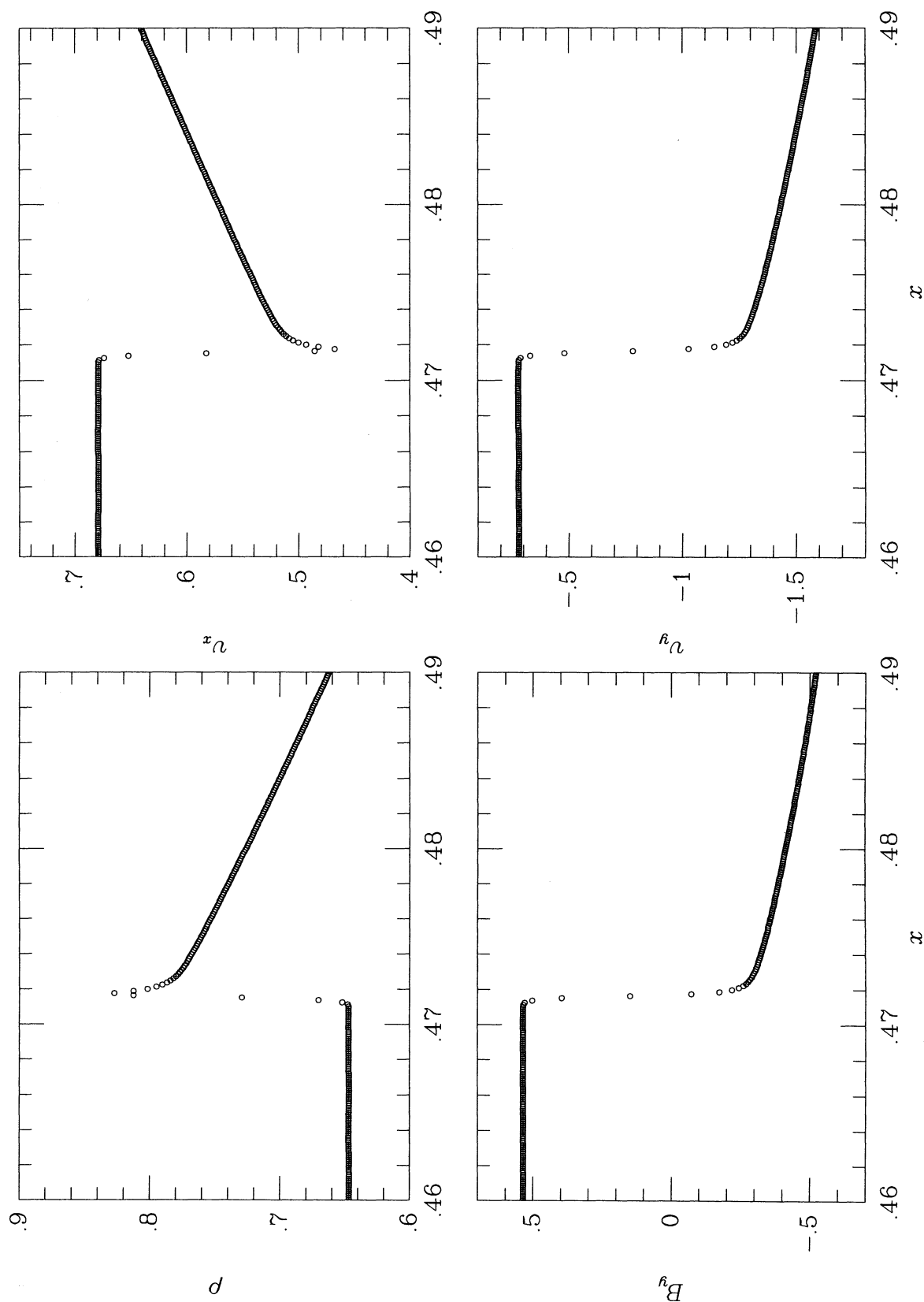


FIG. 6a.—Same slow compound structure in the MHD shock tube test as that in Fig. 5a. The calculation has been done with the MHD-TVD code described in § 2 using 8192 cells, and only the region around the slow compound structure has been plotted. Plots show that the slow compound structure from the numerical calculation is composed of a “2–4” intermediate shock followed by a slow rarefaction.

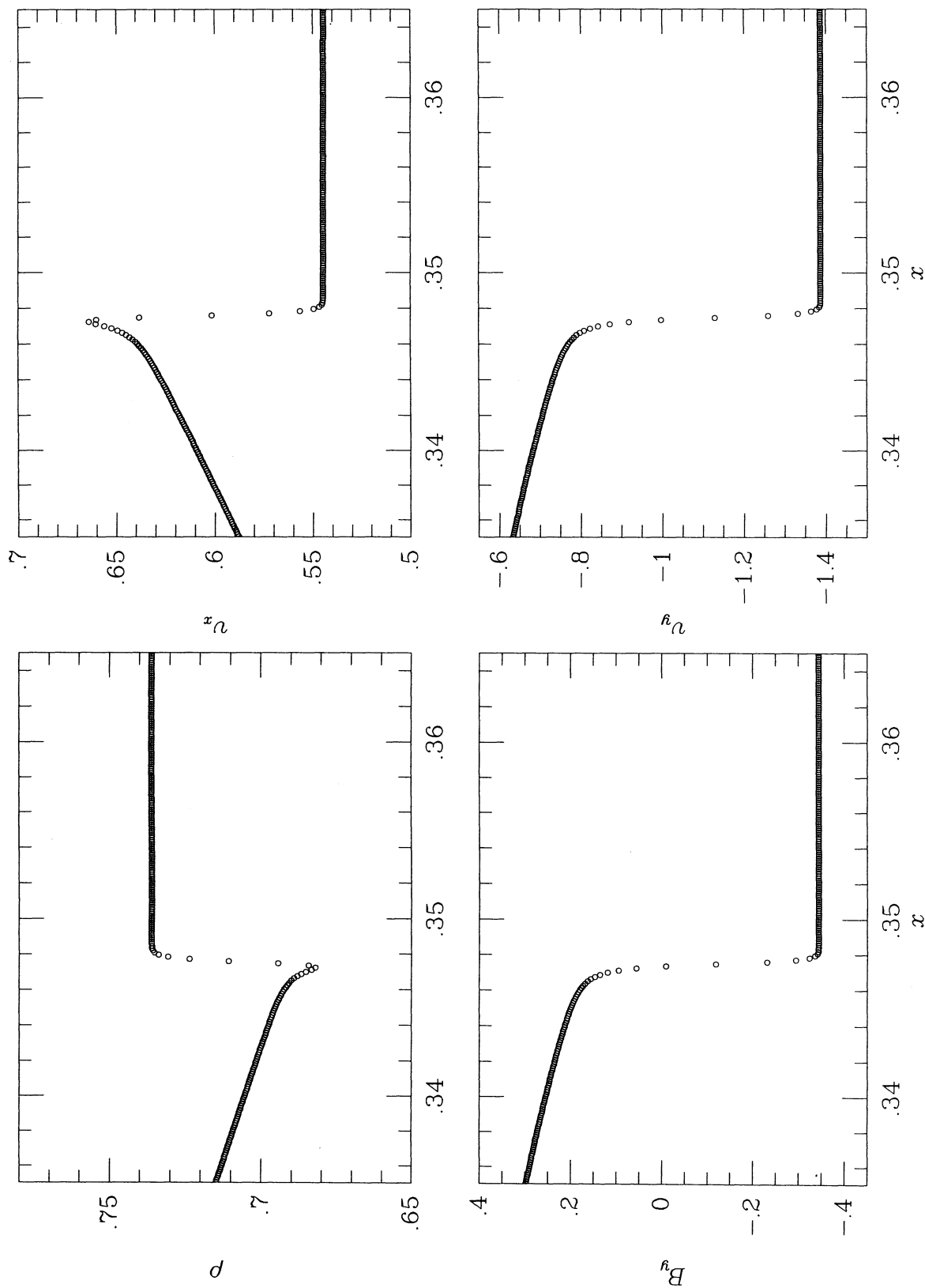


FIG. 6b.—Same fast compound structure in the MHD shock tube test as that in Fig. 5b. The calculation has been done with the MHD-TVD code described in § 2 using 8192 cells and only the region around the fast compound structure has been plotted. Plots show that the fast compound structure from the numerical calculation is composed of a “1–3” intermediate shock preceded by a fast rarefaction.

TABLE 1A  
SHOCK TUBE TEST 1A

$\rho$	$u_x$	$u_y$	$u_z$	$B_y$	$B_z$	$p$
1.0000e+00	1.0000e+01	0.0000e+00	0.0000e+00	1.4105e+00	0.0000e+00	2.0000e+01
2.6797e+00	7.2113e-01	2.3139e-01	0.0000e+00	3.8389e+00	0.0000e+00	1.5098e+02
2.6797e+00	7.2113e-01	2.3139e-01	0.0000e+00	3.8389e+00	0.0000e+00	1.5098e+02
2.6713e+00	7.2376e-01	3.5684e-01	0.0000e+00	4.0380e+00	0.0000e+00	1.5019e+02
3.8508e+00	7.2376e-01	3.5684e-01	0.0000e+00	4.0380e+00	0.0000e+00	1.5019e+02
3.7481e+00	7.0505e-01	-3.8804e-01	0.0000e+00	5.4272e+00	0.0000e+00	1.4357e+02
3.7481e+00	7.0505e-01	-3.8804e-01	0.0000e+00	5.4272e+00	0.0000e+00	1.4357e+02
1.0000e+00	-1.0000e+01	0.0000e+00	0.0000e+00	1.4105e+00	0.0000e+00	1.0000e+00

NOTE.— $B_x = 1.4105E + 00$  (DW Table 6).

TABLE 1B  
SHOCK TUBE TEST 1B

$\rho$	$u_x$	$u_y$	$u_z$	$B_y$	$B_z$	$p$
1.0000e+00	0.0000e+00	0.0000e+00	0.0000e+00	1.4105e+00	0.0000e+00	1.0000e+00
1.9185e+00	-1.6671e+00	3.5507e-01	0.0000e+00	2.8715e+00	0.0000e+00	3.6772e+00
1.9185e+00	-1.6671e+00	3.5507e-01	0.0000e+00	2.8715e+00	0.0000e+00	3.6772e+00
2.8547e+00	-1.8550e+00	-1.2025e+00	0.0000e+00	8.4874e-01	0.0000e+00	7.6462e+00
8.5130e-02	-1.8550e+00	-1.2025e+00	0.0000e+00	8.4874e-01	0.0000e+00	7.6462e+00
8.6823e-02	-1.7992e+00	5.5455e-02	0.0000e+00	4.8640e-01	0.0000e+00	7.9017e+00
8.6823e-02	-1.7992e+00	5.5455e-02	0.0000e+00	4.8640e-01	0.0000e+00	7.9017e+00
1.0000e-01	0.0000e+00	0.0000e+00	0.0000e+00	5.6419e-01	0.0000e+00	1.0000e+01

NOTE.— $B_x = 8.4628E - 01$  (DW Table 3A).

TABLE 2A  
SHOCK TUBE TEST 2A

$\rho$	$u_x$	$u_y$	$u_z$	$B_y$	$B_z$	$p$
1.0800e+00	1.2000e+00	1.0000e-02	5.0000e-01	1.0155e+00	5.6419e-01	9.5000e-01
1.4903e+00	6.0588e-01	1.1235e-01	5.5686e-01	1.4383e+00	7.9907e-01	1.6558e+00
1.4903e+00	6.0588e-01	2.2157e-01	3.0125e-01	1.5716e+00	4.8702e-01	1.6558e+00
1.6343e+00	5.7538e-01	4.7602e-02	2.4734e-01	1.4126e+00	4.3772e-01	1.9317e+00
1.4735e+00	5.7538e-01	4.7601e-02	2.4734e-01	1.4126e+00	4.3772e-01	1.9317e+00
1.3090e+00	5.3432e-01	-1.8411e-01	1.7554e-01	1.6103e+00	4.9899e-01	1.5844e+00
1.3090e+00	5.3432e-01	-9.4572e-02	-4.7286e-02	1.5078e+00	7.5392e-01	1.5844e+00
1.0000e+00	0.0000e+00	0.0000e+00	0.0000e+00	1.1284e+00	5.6419e-01	1.0000e+00

NOTE.— $B_x = 5.6419E - 01$  (DW Table 1A).

TABLE 2B  
SHOCK TUBE TEST 2B

$\rho$	$u_x$	$u_y$	$u_z$	$B_y$	$B_z$	$p$
1.0000e+00	0.0000e+00	0.0000e+00	0.0000e+00	1.6926e+00	0.0000e+00	1.0000e+00
1.7577e+00	-1.5336e+00	3.3873e-01	0.0000e+00	3.1166e+00	0.0000e+00	3.0321e+00
1.7577e+00	-1.5336e+00	2.9068e-01	4.7290e-01	3.0529e+00	6.2695e-01	3.0321e+00
2.8307e+00	-1.7507e+00	-1.2739e+00	1.5159e-01	1.1924e+00	2.4487e-01	7.3663e+00
8.3243e-02	-1.7507e+00	-1.2739e+00	1.5159e-01	1.1924e+00	2.4487e-01	7.3663e+00
8.8226e-02	-1.5878e+00	2.0417e+00	8.3250e-01	2.4227e-01	4.9753e-02	8.1157e+00
8.8226e-02	-1.5878e+00	2.0247e+00	1.0000e+00	2.4732e-01	0.0000e+00	8.1157e+00
1.0000e-01	0.0000e+00	2.0000e+00	1.0000e+00	2.8209e-01	0.0000e+00	1.0000e+01

NOTE.— $B_x = 8.4628E - 01$ .

TABLE 3A  
SHOCK TUBE TEST 3A

$\rho$	$u_x$	$u_y$	$u_z$	$B_y$	$B_z$	$p$
1.0000e-01	5.0000e+01	0.0000e+00	0.0000e+00	-2.8209e-01	-5.6419e-01	4.0000e-01
3.8714e-01	2.5033e+01	0.0000e+00	0.0000e+00	-1.0921e+00	-2.1842e+00	8.1660e+01
3.8714e-01	2.5033e+01	0.0000e+00	0.0000e+00	-1.0921e+00	-2.1842e+00	8.1660e+01
3.8714e-01	2.5033e+01	0.0000e+00	0.0000e+00	-1.0921e+00	-2.1842e+00	8.1660e+01
3.9044e-01	2.5033e+01	0.0000e+00	0.0000e+00	1.1014e+00	2.2029e+00	8.1609e+01
3.9044e-01	2.5033e+01	0.0000e+00	0.0000e+00	1.1014e+00	2.2029e+00	8.1609e+01
3.9044e-01	2.5033e+01	0.0000e+00	0.0000e+00	1.1014e+00	2.2029e+00	8.1609e+01
1.0000e-01	0.0000e+00	0.0000e+00	0.0000e+00	2.8209e-01	5.6419e-01	2.0000e-01

NOTE.— $B_x = 0.0000E + 00$  (DW Table 2A).

TABLE 3B  
SHOCK TUBE TEST 3B

$\rho$	$u_x$	$u_y$	$u_z$	$B_y$	$B_z$	$p$
1.0000e+00	-1.0000e+00	0.0000e+00	0.0000e+00	1.0000e+00	0.0000e+00	1.0000e+00
4.9653e-01	1.2673e-07	0.0000e+00	0.0000e+00	4.9638e-01	0.0000e+00	3.1134e-01
4.9653e-01	1.2673e-07	0.0000e+00	0.0000e+00	4.9638e-01	0.0000e+00	3.1134e-01
4.9653e-01	1.2673e-07	0.0000e+00	0.0000e+00	4.9638e-01	0.0000e+00	3.1134e-01
4.9653e-01	-1.2673e-07	0.0000e+00	0.0000e+00	4.9638e-01	0.0000e+00	3.1134e-01
4.9653e-01	-1.2673e-07	0.0000e+00	0.0000e+00	4.9638e-01	0.0000e+00	3.1134e-01
4.9653e-01	-1.2673e-07	0.0000e+00	0.0000e+00	4.9638e-01	0.0000e+00	3.1134e-01
1.0000e+00	1.0000e+00	0.0000e+00	0.0000e+00	1.0000e+00	0.0000e+00	1.0000e+00

NOTE.— $B_x = 0.0000E + 00$ .

TABLE 4A  
SHOCK TUBE TEST 4A

$\rho$	$u_x$	$u_y$	$u_z$	$B_y$	$B_z$	$p$
1.0000e+00	0.0000e+00	0.0000e+00	0.0000e+00	1.0000e+00	0.0000e+00	1.0000e+00
5.9955e-01	8.1237e-01	-5.9961e-01	0.0000e+00	2.8431e-01	0.0000e+00	4.2629e-01
5.9955e-01	8.1237e-01	-5.9961e-01	0.0000e+00	2.8431e-01	0.0000e+00	4.2629e-01
5.5151e-01	8.9416e-01	-5.4470e-01	0.0000e+00	3.1528e-01	0.0000e+00	3.7090e-01
4.1272e-01	8.9416e-01	-5.4470e-01	0.0000e+00	3.1528e-01	0.0000e+00	3.7090e-01
2.2337e-01	2.4722e-01	-9.1164e-01	0.0000e+00	4.3086e-01	0.0000e+00	1.2402e-01
2.2337e-01	2.4722e-01	-9.1164e-01	0.0000e+00	4.3086e-01	0.0000e+00	1.2402e-01
2.0000e-01	0.0000e+00	0.0000e+00	0.0000e+00	0.0000e+00	0.0000e+00	1.0000e-01

NOTE.— $B_x = 1.0000E + 00$ .

TABLE 4B  
SHOCK TUBE TEST 4B

$\rho$	$u_x$	$u_y$	$u_z$	$B_y$	$B_z$	$p$
4.0000e-01	-6.6991e-01	9.8263e-01	0.0000e+00	2.5293e-03	0.0000e+00	5.2467e-01
4.0000e-01	-6.6991e-01	9.8263e-01	0.0000e+00	2.5305e-03	0.0000e+00	5.2467e-01
4.0000e-01	-6.6991e-01	9.8263e-01	0.0000e+00	2.5305e-03	0.0000e+00	5.2467e-01
4.0000e-01	-6.6991e-01	9.8263e-01	0.0000e+00	2.5305e-03	0.0000e+00	5.2467e-01
6.7910e-01	-6.6991e-01	9.8263e-01	0.0000e+00	2.5305e-03	0.0000e+00	5.2467e-01
6.7910e-01	-6.6991e-01	9.8263e-01	0.0000e+00	2.5304e-03	0.0000e+00	5.2467e-01
6.7910e-01	-6.6991e-01	9.8263e-01	0.0000e+00	2.5304e-03	0.0000e+00	5.2467e-01
1.0000e+00	0.0000e+00	0.0000e+00	0.0000e+00	1.0000e+00	0.0000e+00	1.0000e+00

NOTE.— $B_x = 1.3000E + 00$ .

TABLE 4C  
SHOCK TUBE TEST 4C

$\rho$	$u_x$	$u_y$	$u_z$	$B_y$	$B_z$	$p$
6.5000e-01	6.6700e-01	-2.5700e-01	0.0000e+00	5.5000e-01	0.0000e+00	5.0000e-01
6.6033e-01	6.4419e-01	-2.4521e-01	0.0000e+00	5.6490e-01	0.0000e+00	5.1331e-01
6.6033e-01	6.4419e-01	-2.4521e-01	0.0000e+00	5.6490e-01	0.0000e+00	5.1331e-01
8.4693e-01	4.4085e-01	-9.4017e-01	0.0000e+00	1.8817e-04	0.0000e+00	7.9679e-01
1.0370e+00	4.4085e-01	-9.4017e-01	0.0000e+00	1.8817e-04	0.0000e+00	7.9679e-01
1.0370e+00	4.4085e-01	-9.4000e-01	0.0000e+00	1.0666e-05	0.0000e+00	7.9679e-01
1.0370e+00	4.4085e-01	-9.4000e-01	0.0000e+00	1.0666e-05	0.0000e+00	7.9679e-01
1.0000e+00	4.0000e-01	-9.4000e-01	0.0000e+00	1.0000e-05	0.0000e+00	7.5000e-01

NOTE.— $B_x = 7.5000E - 01$ .

TABLE 4D  
SHOCK TUBE TEST 4D

$\rho$	$u_x$	$u_y$	$u_z$	$B_y$	$B_z$	$p$
1.0000e+00	0.0000e+00	0.0000e+00	0.0000e+00	1.0000e-03	0.0000e+00	1.0000e+00
9.4010e-01	7.8931e-02	-4.8369e-05	0.0000e+00	9.1439e-04	0.0000e+00	9.0217e-01
9.4010e-01	7.8931e-02	-1.6443e-04	4.5325e-04	8.0186e-04	4.3947e-04	9.0217e-01
6.5148e-01	3.2269e-01	8.0687e-01	4.4276e-01	6.6037e-01	3.6192e-01	4.8959e-01
4.9728e-01	3.2268e-01	8.0687e-01	4.4276e-01	6.6037e-01	3.6192e-01	4.8959e-01
2.9771e-01	-1.8369e-02	2.3358e-01	1.2856e-01	8.6757e-01	4.7548e-01	1.9746e-01
2.9771e-01	-1.8369e-02	1.0432e-02	1.0000e+00	9.8933e-01	0.0000e+00	1.9746e-01
3.0000e-01	0.0000e+00	0.0000e+00	1.0000e+00	1.0000e+00	0.0000e+00	2.0000e-01

NOTE.— $B_x = 7.0000E - 01$ .

TABLE 5A  
SHOCK TUBE TEST 5A

$\rho$	$u_x$	$u_y$	$u_z$	$B_y$	$B_z$	$p$
1.0000e+00	0.0000e+00	0.0000e+00	0.0000e+00	1.0000e+00	0.0000e+00	1.0000e+00
6.5673e-01	6.5790e-01	-2.6700e-01	0.0000e+00	5.4966e-01	0.0000e+00	4.9618e-01
6.5673e-01	6.5790e-01	-1.6235e+00	0.0000e+00	-5.4966e-01	0.0000e+00	4.9618e-01
6.6535e-01	6.4841e-01	-1.6053e+00	0.0000e+00	-5.3799e-01	0.0000e+00	5.0709e-01
2.7400e-01	6.4841e-01	-1.6053e+00	0.0000e+00	-5.3799e-01	0.0000e+00	5.0709e-01
1.1571e-01	-2.7717e-01	-1.9847e-01	0.0000e+00	-8.8576e-01	0.0000e+00	8.7927e-02
1.1571e-01	-2.7717e-01	-1.9847e-01	0.0000e+00	-8.8576e-01	0.0000e+00	8.7927e-02
1.2500e-01	0.0000e+00	0.0000e+00	0.0000e+00	-1.0000e+00	0.0000e+00	1.0000e-01

NOTE.— $B_x = 7.5000E - 01$  (BW, except  $\gamma = 5/3$ ; DW Table 4A).

TABLE 5B  
SHOCK TUBE TEST 5B

$\rho$	$u_x$	$u_y$	$u_z$	$B_y$	$B_z$	$p$
1.0000e+00	0.0000e+00	0.0000e+00	0.0000e+00	1.0000e+00	0.0000e+00	1.0000e+00
7.2751e-01	5.5942e-01	-5.7673e-01	0.0000e+00	3.4899e-01	0.0000e+00	5.8848e-01
7.2751e-01	5.5942e-01	-1.3951e+00	0.0000e+00	-3.4899e-01	0.0000e+00	5.8848e-01
9.1190e-01	3.0152e-01	-1.2382e+00	0.0000e+00	-2.3702e-01	0.0000e+00	8.6059e-01
6.0378e-01	3.0152e-01	-1.2382e+00	0.0000e+00	-2.3702e-01	0.0000e+00	8.6059e-01
3.2246e-01	-5.5835e-01	-7.9046e-01	0.0000e+00	-4.4197e-01	0.0000e+00	2.7931e-01
3.2246e-01	-5.5835e-01	-7.9046e-01	0.0000e+00	-4.4197e-01	0.0000e+00	2.7931e-01
4.0000e-01	0.0000e+00	0.0000e+00	0.0000e+00	-1.0000e+00	0.0000e+00	4.0000e-01

NOTE.— $B_x = 1.3000E + 00$ .

In the fourth test set, we examine how the MHD-TVD code and the Riemann solver deal with a special category of fast and slow structures, namely, the so-called switch-on and switch-off structures. The tangential magnetic field turns on in the region behind switch-on fast shocks and switch-on slow rarefactions. On the other hand, it turns off in the region behind switch-off slow shocks and switch-off fast rarefactions. The test involving a switch-on fast shock has been set up with the left state  $(\rho, v_x, v_y, v_z, B_y, B_z, E) = (1, 0, 0, 0, 1, 0, 1)$  and the right state  $(0.2, 0, 0, 0, 0, 0, 0.1)$  and with  $B_x = 1$ . The switch-on fast shock propagates to the right. Other structures formed in this test include a fast rarefaction, a slow rarefaction, a contact discontinuity, and a slow shock. The test results are plotted at time  $t = 0.15$  in Figure 4a, showing that the code and the Riemann solver handle the switch-on fast shock without any trouble.

The test involving a switch-off fast rarefaction has been set up with the left state  $(\rho, v_x, v_y, v_z, B_y, B_z, E) = (0.4, -0.66991, 0.98263, 0, 0.0025293, 0, 0.52467)$  and the right state  $(1, 0, 0, 0, 1, 0, 1)$  and with  $B_x = 1.3$ . It has been designed to generate only a right-moving, switch-off fast rarefaction, and a contact discontinuity with an accuracy (the ratio of residual strength to prerarefaction strength of the tangential magnetic field) better than 0.3% (see Table 4B). The test results are plotted at time  $t = 0.15$  in Figure 4b. The numerical calculation shows small, yet noticeable, signatures of the right-moving slow structure and the left-moving hydrodynamic structure.

The test involving a switch-off slow shock has been set up with the left state  $(\rho, v_x, v_y, v_z, B_y, B_z, E) = (0.65, 0.667, -0.257, 0, 0.55, 0, 0.5)$  and the right state  $(1, 0.4, -0.94, 0, 0, 0, 0.75)$  and with  $B_x = 0.75$ . The solution of this test has, from left to right, a fast shock, a switch-off slow shock, a contact discontinuity, and a hydrodynamic shock. In the region to the right of the switch-off slow shock, the structures are almost hydrodynamic because the tangential magnetic field is very small. The test results are plotted at time  $t = 0.15$  in Figure 4c, showing good agreement between the numerical calculation and the analytic solution. Our Riemann solver turns off the tangential magnetic field in this case to an accuracy of about 0.04% as indicated in Table 4C.

The test involving a switch-on slow rarefaction has been set up with the left state  $(\rho, v_x, v_y, v_z, B_y, B_z, E) = (1, 0, 0, 0, 0, 0, 1)$  and the right state  $(0.3, 0, 0, 1, 1, 0, 0.2)$  and with  $B_x = 0.7$ . The structures formed in this test include a hydrodynamic rarefaction, a switch-on slow shock, a contact discontinuity, a slow shock, a rotational discontinuity, and a fast rarefaction. With the hydrodynamic nature in the region between the two left-moving rarefactions, no rotational discontinuity is produced on the left side of the contact discontinuity. Hence this test has a solution with only one rotational discontinuity, while two discontinuities are expected in most tests with three-dimensional field structure (e.g., the tests in Fig. 2). The test results are plotted at time  $t = 0.16$  in Figure 4d. The noticeable kink in  $\psi$  in this plot is the results of the smoothed foot in the switch-on rarefaction wave and the artificial set to  $\psi = 0$  for  $B_z < 10^{-3}$ .

The final set of tests involves so-called compound structures; that is, structures that involve a shock and a rarefaction of the same wave family moving together. Their existence was first discussed in BW. The initial setups for such waves include two-dimensional field and velocity structures in the  $x$ - $y$  plane such that the sign of the tangential magnetic field ( $B_y$ ) changes across the initial discontinuity. The test involving a slow compound structure has been set up with the left state  $(\rho, v_x, v_y, v_z, B_y, B_z, E) = (1, 0, 0, 0, 1, 0, 1)$  and the right state  $(0.125, 0, 0, 0, -1, 0, 0.1)$  and with  $B_x = 0.75$ . It is the same test as in BW, except we set the adiabatic index,  $\gamma = 5/3$ , instead of  $\gamma = 2$ . The results are plotted at time  $t = 0.1$  in Fig. 5a. Here lines are the solution of the Riemann solver which has a rotational discontinuity and a slow shock instead of a slow compound structure, and numerical values of the solution are listed in Table 5a. Clearly the numerical calculations and the analytic solution produce different results around the compound structure, even though the agreement in other structures: two fast rarefactions, a slow shock, and a contact discontinuity, is acceptable for most purposes. That same difference has been seen in all previously reported simulations (e.g., BW; Stone et al. 1992; DW).

Similarly, we set up a test involving a fast compound with the left state  $(\rho, v_x, v_y, v_z, B_y, B_z, E) = (1, 0, 0, 0, 1, 0, 1)$  and the right state  $(0.4, 0, 0, 0, -1, 0, 0.4)$  and with  $B_x = 1.3$ . The results are plotted at time  $t = 0.16$  in Figure 5b. Again lines are the solution of the Riemann solver with a rotational discontinuity and a fast rarefaction instead of a fast compound structure, and numerical values of the solution are listed in Table 5b. Further discussion on compound structures will follow in the next section.

In summary, the above tests with MHD shock tube problems produce general and detailed agreement between the numerical calculations and the analytic solutions. The comparisons are entirely satisfactory, except in the tests involving compound structures. Especially, the positions of shocks, rarefactions, and discontinuities agree very well, indicating they both generate the same solutions. Numerical results show that our code resolves strong shocks (fast, slow, or magnetosonic) typically with two to four cells, but more cells are required for weaker shocks with a smaller jump in the parallel flow velocity. Rotational discontinuities are resolved with three to five cells with proper steepening, but contact discontinuities are resolved with  $\sim 10$  cells without steepening. Tangential discontinuities spread over  $\sim 15$  cells. Further work could be done to develop proper steepening schemes for contact discontinuities and tangential discontinuities to improve the ability of the MHD-TVD code to handle these discontinuities.

#### 5. DISCUSSION

We return now briefly to the issues surrounding the formation of compound waves. The BW test problem involving a slow compound wave (Fig. 5a) has attracted considerable attention. It is related to structures known as “intermediate” shocks (e.g., Wu 1988; Kennel, Blandford, & Wu 1990). Such shocks reverse the direction of  $B_\perp$  and lead to a flow that passes from super-Alfvénic to sub-Alfvénic; thus, the name. Recall from the above comments that in both the BW compound wave and the fast compound wave shown in Figure 5b, the field changes direction; i.e., the sign of  $\psi$  reverses. In addition, the flow makes the super-Alfvénic to sub-Alfvénic transition in crossing the compound wave. As mentioned above, numerical MHD codes, which are always dissipative, seem generally to find the BW compound structure out of that particular shock-tube initial condition instead of introducing a rotation in the magnetic field plane. For the compound wave it does not appear necessary that the magnetic field anywhere exist outside the upstream or downstream field plane. Thus, it would appear that this structure might be represented as a “ $1 + \frac{1}{2}$ ”-dimensional flow problem”. However, ideal MHD Riemann solvers that allow rotational discontinuities will generally find a



solution to that shock-tube problem that interprets the compound structure as a rotational discontinuity followed by a slow shock, making it a " $1 + \frac{1}{2} + \frac{1}{2}$ -dimensional" flow.

It is not our intent to add to the controversy surrounding the reality of intermediate shocks. However, there is some interest in the community on the properties of these transitions. For that reason and to test the performance and properties of our code, we have done a high-resolution calculation for the test of the slow compound structure in Figure 5a with 8192 cells. The magnified region around the slow compound structure has been plotted in Figure 6a. From the plot, the numerical values of several flow quantities on both sides of the "shock" read as follows:  $\rho = 0.647$  (density),  $p_g = 0.484$  (gas pressure),  $u = 0.963$  (flow velocity in the shock frame),  $B_y = 0.536$  (tangential magnetic field),  $c_f = 1.423$  (fast speed),  $c_a = 0.932$  (Alfvén speed),  $c_s = 0.732$  (slow speed),  $a = 1.117$  (sound speed) in the preshock region,  $\rho = 0.827$ ,  $p_g = 0.758$ ,  $u = 0.751$ ,  $B_y = -0.0738$ ,  $c_f = 1.241$ ,  $c_a = 0.825$ ,  $c_s = 0.822$ ,  $a = 1.236$  in the postshock region, and shock velocity in lab frame is 0.284. In the preshock region the flow velocity is  $c_a < u < c_f$  (subfast but super-Alfvénic) with Alfvénic Mach number  $M_a = 1.03$ , while in the postshock region  $u < c_s$  (subslow) with  $M_a = 0.910$ . Hence, the shock in the numerical calculation with our code should be considered as a 2–4 intermediate shock and the slow compound structure as an intermediate shock followed by a slow rarefaction.

We have done also a high-resolution calculation for the test of the fast compound structure in Figure 5b with 8192 cells, and the magnified region around the fast compound structure has been plotted in Figure 6b. The numerical values in the plot of several flow quantities on the both sides of the "shock" read as follows:  $\rho = 0.6820$ ,  $p_g = 0.5290$ ,  $u = 1.617$ ,  $B_y = 0.0555$ ,  $c_f = 1.577$ ,  $c_a = 1.574$ ,  $c_s = 1.135$ ,  $a = 1.137$  in the preshock region,  $\rho = 0.7361$ ,  $p_g = 0.6031$ ,  $u = 1.498$ ,  $B_y = -0.3442$ ,  $c_f = 1.622$ ,  $c_a = 1.515$ ,  $c_s = 1.092$ ,  $a = 1.169$  in the postshock region, and shock velocity in lab frame is 0.935. In the preshock region the flow velocity is  $u > c_f$  (superfast) with  $M_a = 1.027$ , while in the postshock region  $c_s < u < c_a$  (sub-Alfvénic but superslow) with  $M_a = 0.989$ . Hence, the shock in the numerical calculation with our code should be considered as a 1–3 intermediate shock and the fast compound structure as a intermediate shock preceded by a fast rarefaction.

The work by D. R. was supported in part by a David and Lucille Packard Foundation Fellowship through Jeremy Goodman at Princeton University and in part by Non-Directed Research Fund of Korea Research Foundation 1993 at Chungnam National University. Work by T. W. J. was supported in part by NASA through grant NAGW-2548, the NSF through grant AST 91-00486, by a travel grant from the University of Minnesota International Programs Office, and by the University of Minnesota Super-computer Institute (UMSI). The UMSI also generously contributed support for travel by D. R.

#### REFERENCES

- |  |  |
|--|--|
| <p>Brio, M., &amp; Wu, C. C. 1988, <i>J. Comput. Phys.</i>, 75, 500 (BW)</p> <p>Colella, P., &amp; Woodward, P. R. 1984, <i>J. Comput. Phys.</i>, 54, 174</p> <p>Dai, W., &amp; Woodward, P. R. 1994a, <i>J. Comput. Phys.</i>, 111, 354 (DW)</p> <p>———. 1994b, preprint</p> <p>DeVore, C. R. 1991, <i>J. Comput. Phys.</i>, 92, 142</p> <p>Harten, A. 1983, <i>J. Comput. Phys.</i>, 49, 357</p> <p>Jeffrey, A. 1966, <i>Magnetohydrodynamics</i> (London: Oliver &amp; Boyd)</p> <p>Jeffrey, A., &amp; Taniuti, T. 1964, <i>Nonlinear Waves Propagation</i> (New York: Academic)</p> <p>Kennel, C. F., Blandford, R. D., &amp; Wu, C. C. 1990, <i>Phys. Fluids B</i>, 2, 253</p> <p>Lind, K. R., Payne, D. G., &amp; Meier, D. L. 1991, unpublished</p> | <p>Parker, E. N. 1979, <i>Cosmical Magnetic Fields: Their Origin and Their Activity</i> (Oxford: Oxford Univ. Press).</p> <p>Roe, P. L. 1981, <i>J. Comput. Phys.</i>, 43, 357</p> <p>Shu, F. H. 1992, <i>The Physics of Astrophysics</i>, Vol. 2, Gas Dynamics (Mill Valley: University Science Books)</p> <p>Stone, J. M., Hawley, J. F., Evans, C. R., &amp; Norman, M. L. 1992, <i>ApJ</i>, 388, 415</p> <p>Stone, J. M., &amp; Norman, M. L. 1992, <i>ApJS</i>, 80, 791</p> <p>Wu, C. C. 1988, <i>J. Geophys. Res.</i>, 93, 987</p> <p>Zachary, A. L., &amp; Colella, P. 1992, <i>J. Comput. Phys.</i>, 99, 341</p> <p>Zachary, A. L., Malagoli, A., &amp; Colella, P. 1994, <i>SIAM J. Sci. Comp.</i>, 15, 263</p> |
|--|--|